Exploring Regional Climate of the Euro-Mediterranean Using a Variable-Resolution Configuration of the Global Community Earth System Model (VR-CESM)

Burcu Boza[1], Adam Herrington[2], Mehmet Ilicak[1], Gokhan Danabasoglu[2], and Omer Lutfi Sen[1]

[1] Istanbul Technical University, Eurasia Institute of Earth Sciences, Istanbul, Türkiye.

[2] US National Science Foundation National Center for Atmospheric Research, Boulder, CO, USA.

Corresponding author: Burcu Boza (boza21@itu.edu.tr)

Key Points:

- Fidelity of VR-CESM simulations with highest resolutions of 0.25° and 0.125° is evaluated for near-surface air temperature and precipitation
- VR-CESM accurately represents near-surface air temperature and precipitation especially over complex topography
- VR-CESM may be preferred over regional climate models to investigate the Euro-Mediterranean's climate

Abstract

A Variable-Resolution, global configuration of the Community Earth System Model (VR-CESM) in which the atmosphere and land are the only active components is employed to investigate the climate of the Euro-Mediterranean region. Two variable-resolution grids with regionally-refined resolutions of 0.25° and 0.125° over the study domain, respectively, are used. The fidelity of these VR-CESM simulations is evaluated considering the near-surface air temperature and precipitation fields for the 2000-2014 period in comparison to available observation-based datasets and those of a coarse resolution (quasi-uniform 1°) control simulation. Our analysis shows that, as a global model, VR-CESM is a promising alternative to regional climate models to advance our understanding of the Euro-Mediterranean climate. The improvements obtained are mainly related to a better representation of the complex topography of the region with higher resolution. Increasing the regional resolution to 0.25° generally yields considerable improvements over the control simulation, however some persistent biases remain. Doubling the highest resolution to 0.125° leads to only modest improvements, primarily in the representation of small-scale processes including representation of extreme events that are of substantial relevance for the present and future of the regional climate.

Plain Language Summary

The Euro-Mediterranean region has a highly complex and distinctive climatology making the simulation of the regional climate a challenging task. The region is influenced by several large-scale circulation patterns, requiring a global modeling framework. At the same time, due to its rather complex topography, models need high spatial resolution to represent many small-scale climatic features of the region. To address this challenge, we employ a variable-resolution configuration of the Community Earth System Model (VR-CESM) with a high resolution over this region within a global model which has lower resolution elsewhere. We show that VR-CESM simulations produce better representations of precipitation and surface temperature, especially over complex topography, in comparison to a control simulation with no resolution enhancement over the region.

1 Introduction

The Euro-Mediterranean region lies in a transitional zone between arid and subarctic climates, mainly including arid, Mediterranean, oceanic and humid continental climates (Kottek et al., 2006). It is influenced by large-scale circulation patterns such as the Icelandic Low, the Siberian High, the Azores High, and the South Asian Monsoon as well as by teleconnection patterns such as the El Niño Southern Oscillation and the Arctic Oscillation, among others (Sen et al., 2019). The climate of the Mediterranean Basin is characterized by high seasonality as it has a typical winter maximum in precipitation, in contrast with humid climate of Europe, which features rainy conditions all year around. The presence of inland seas, land-sea contrast, complex topography, and coastlines of the region all have a strong modulating effect on large-scale patterns leading to many meso-beta scale climatic features locally. The region contains two large semi-enclosed seas: the Mediterranean Sea and the Black Sea – the former with a connection to the Atlantic Ocean through the narrow Gibraltar Strait. Together with the surrounding high mountain chains, these two seas create sharp land-sea contrasts. The Mediterranean Sea is, in particular, a major source of heat and moisture for the surrounding areas, and it is large enough to host both subtropical cyclones and tropical-like cyclones called the medicanes (Fita et al., 2007). For detailed information on the main characteristics of the regional climate and the spatial patterns of seasonal precipitation and surface temperature, the reader is referred to Lionello et al. (2006) and Xoplaki (2002), respectively.

The Mediterranean Basin is a climate change hotspot (Giorgi, 2006) with a projected regional warming above global means and reduced rainfall. These projected warmer and drier conditions threaten human population and ecosystems in the region. Highly interconnected climate risks include water scarcity, water and food security, risks related to droughts, floods, heat waves and wildfires, and ecosystem losses. The Euro-Mediterranean region is frequently affected by extreme climate events such as heat waves, cold spells, heavy precipitation, and windstorms, and these events are generally projected to intensify, become more frequent and longer in the future. These vulnerabilities of the region add to the importance and urgency of better understanding the mesoscale and large-scale dynamics that determine the regional present-day climate. Considering their large-scale links (Bozkurt et al., 2019; Insua-Costa et al., 2022; Toreti et al., 2010), taking a global perspective is even more important for extreme events.

With its unique characteristics, modeling the Euro-Mediterranean region's climate is a challenging task. Reliable and robust simulations with an adequate spatiotemporal resolution to resolve sharp regional gradients (Onol & Semazzi, 2009), such as the precipitation and temperature differences occurring over short distances due to the region's mountainous topography, are needed. At the same time, model simulations are expected to adequately represent global and regional teleconnections, large-scale circulation patterns, and multi-scale interactions driving the regional climate. Uniform high-resolution (0.1°-0.25°) general circulation models (GCMs) could be used to address these challenges (e.g., Small et al., 2014), but their routine use would be prohibitively expensive due to substantial computational costs.

An alternative is to employ downscaling with high-resolution regional climate models (RCMs). While RCMs allow region-specific tunings to simulate regional climates more realistically, which is not possible with GCMs (Gutowski et al., 2020; Mauritsen et al., 2012), they employ boundary conditions from other global models or reanalysis products, and thus inherit biases from those, and more importantly, they generally lack two-way interactions (Lionello et al., 2006; Raisanen et al., 2004; Rummukainen, 2015). Both of these issues can lead

to inconsistencies between the global and regional scales which can be exacerbated by use of different parameterizations in the global and regional models (Chen, 2002; Ringler et al., 2011; Wang et al., 2004). Indeed, these challenges have been identified in studies that investigated the climate of the Euro-Mediterranean region with RCMs (e.g., Kotlarski et al., 2014). For example, Bergant et al. (2007) investigated the systematic errors in the simulation of the European climate with the Abdus Salam International Centre for Theoretical Physics Regional Climate Model version 3 (ICTP-RegCM3) driven by the reanalysis product from the National Centers for Environmental Prediction (NCEP) and NCAR (NCEP/NCAR reanalysis), and found that most of the systematic errors in the RegCM3 simulation can be related to boundary conditions. They also reported that RCMs cannot correct the biases in the data that they are driven by, but only add regional details to the large-scale information (Fan et al., 2014; Feser et al., 2011). In another study, Onol and Semazzi (2009) investigated the potential role of global warming in modulating the future climate over the eastern Mediterranean region by also employing ICTP-RegCM3 to downscale the present and future climate scenario simulations generated by the National Aeronautics and Space Administration's (NASA) finite-volume atmospheric GCM (fvGCM). They pointed out that the drier summer conditions simulated by the model were inherited by RegCM3 through the lateral boundary conditions from the fvGCM simulation, which was also very dry during summers. The study also found a high level of agreement between the RegCM3 and fvGCM circulation changes. While this finding indicates that the distortion of flow across the lateral boundaries is rather small – a positive aspect for regional model configuration, it emphasizes that RCMs inherit features of boundary conditions from GCMs. Another example is provided by Bozkurt et al. (2012) which downscaled the outputs of three GCMs and a reanalysis dataset using RegCM3 to assess the capability of the regional model in simulating the present-day climatology of the eastern Mediterranean – Black Sea region. In their study, they, too, highlighted the propagation of the GCM features to the large-scale fields generated by the RCM simulation.

Variable-resolution (VR) models, which allow regional refinement within a global framework, offer a promising alternative to other fine-resolution modeling approaches discussed above for investigating regional climates and can be thought of as a bridge between the costly uniform high-resolution models and regional models with their challenges. Indeed, the Community Earth System Model (CESM) provides such an option with its VR atmosphere and land components denoted as VR-CESM. It can be configured easily to increase model resolution in regions of interest. To date, VR-CESM has been successfully used in various studies that include investigations of the orographic forcing and snowpack in Sierra Nevada (Rhoades et al., 2015), Greenland ice sheet surface mass balance (van Kampenhout et al., 2019), wind speed in California (Wang et al., 2020), tropical cyclones (Reed et al., 2012; Zarzycki, Jablonowski, & Taylor, 2014), mean climatology of near-surface temperature and precipitation over California (Huang et al., 2016), climate of the Tibetan Plateau (Rahimi et al., 2019), and atmospheric rivers (Rhoades et al., 2020).

In this paper, we present the very first application of VR-CESM to study the present-day climate over the Euro-Mediterranean region. The fidelity of the simulations will be evaluated considering primarily the near-surface (2-m) air temperature and precipitation fields for the 2000-2014 period against available observation-based datasets, as they are essential variables for describing climate, have direct impacts on human and ecosystems, and are important indicators for climate change. The performance of the fine resolution refinement will be compared to that of a coarse resolution (quasi-uniform 1°) control simulation across daily, monthly, seasonal, and

annual time scales. We also explore the representation of extreme maximum temperature and precipitation with high resolution, motivated by the known skill of high spatiotemporal resolution in simulating such extreme events more realistically (Gutowski et al., 2020) and by the ability of VR-CESM in reproducing extreme statistics from high-resolution simulations (Gettelman et al., 2018). We also present findings from a parameter tuning experiment we carried out to investigate how calibration of some cloud radiative parameters influences the representation of longwave- and shortwave-cloud forcings.

The manuscript is organized as follows. In section 2, the model and methodology along with evaluation datasets are provided. Section 3 is devoted to the presentation and interpretation of results, followed by section 4 that summarizes our findings and conclusions.

2 Model and Evaluation Methodology

2.1 Model

CESM is a fully coupled global Earth system model developed and maintained by the National Science Foundation National Center for Atmospheric Research (NSF NCAR) with contributions from many researchers from universities and other institutions (https://www.cesm.ucar.edu/models/cesm2/). In this study, CESM2.2 version is used (Danabasoglu et al., 2020) in its Atmospheric Model Intercomparison Project (AMIP) setup in which the Community Atmosphere Model version 6.3 (CAM6; Bogenschutz et al., 2018; Gettelman et al., 2019) is the atmosphere component and the Community Land Model version 5 (CLM5; Lawrence et al., 2019) with satellite phenology is the land component. This AMIP configuration is run with prescribed historical sea surface temperatures (SSTs) and sea ice concentrations rather than active ocean and sea-ice components (even so, the sea-ice component, CICE (Hunke et al., 2015), uses a prognostic thermodynamic model). The merged Hadley-OI, based on the monthly-mean Hadley Centre sea ice and SST dataset version 1 (HadISST1) and version 2 of the National Oceanic and Atmospheric Administration (NOAA) weekly optimum interpolation (OI) SST analysis, is used as the surface boundary forcing dataset (Hurrell et al., 2008).

CAM6 employs the unified turbulence scheme, Cloud Layers Unified by Binormals (CLUBB; Golaz et al. 2002; Larson, 2017), which is a prognostic moist turbulence scheme, and an improved two-moment prognostic cloud microphysics, the Morrison and Gettelman microphysics scheme version 2 (MG2; Gettelman & Morrison, 2015). Prognostic rainfall and snowfall capability of the MG2 scheme substantially improves accuracy of mountainous hydroclimate simulations at grid-spacings of < 28 km (Rhoades et al., 2018) where fallout duration of hydrometeors is longer than that of horizontal transport duration across the model grid (Rahimi et al., 2019). The model uses hybrid sigma coordinates with 32 terrain-following vertical levels. The lowest model level is at approximately 60 m, and top of the model is at 3.64 hPa (~40 km).

We employ the Spectral Element dynamical core option (CAM-SE) of CAM6. This hydrostatic dynamical core, which offers VR functionality, is available as an out-of-the-box feature for the first time in CESM2.2. It has many attractive accuracy and conservation features for high-resolution and VR applications, allowing regional dynamical downscaling (or regional grid refinement) within a global context. Here, we briefly present some of these and refer to Dennis et al. (2012), Lauritzen et al. (2018), and Taylor and Fournier (2010) for further details.

Spectral element method, which is designed for unstructured grids, offers geometric flexibility of finite element methods and high-order accuracy and mesh convergence properties of spectral methods (Dennis et al., 2012). CAM-SE is based on nonoverlapping quasi-uniform grids (spectral elements). Therefore, numerical instability arising from polar convergence of meridians in traditional latitude-longitude (finite-volume) grids, the so-called 'pole problem', is not an issue (Herrington et al., 2022). In CAM-SE, the primitive equations of motion are solved on individual elements. Hence, CAM-SE is a highly scalable dynamical core and well suited for high-resolution simulations by utilizing today's parallel computing opportunities. It uses dry-mass hybrid vertical coordinates which simplifies the representation of mass effects of moisture and condensates in thermodynamic and momentum equations, that is, in the dynamical core, which is also particularly important in high resolutions (Bacmeister et al., 2012). Such dry-mass vertical coordinates offer consistent coupling with physical parametrizations and better treatment of total energy conservation (Lauritzen et al., 2018).

In CAM-SE, a fourth-order hyper-viscosity is applied for horizontal diffusion (Dennis et al., 2012). Tensor hyper-viscosity, a mechanism for the dissipation of grid scale variance of multi-resolution grids, is only active in VR configurations (Guba et al., 2014). Tensor hyper-viscosity coefficients scale independently for both length scales of quadrilateral elements instead of using a constant coefficient based on a single length scale. This leads to a smoother transition between different resolutions and avoids artifacts in the transition regions.

VR-CESM takes advantage of CAM-SE's increased grid flexibility (Zarzycki, Jablonowski, & Taylor, 2014). With the ability of using unstructured grids, VR-CESM allows grid refinement by smooth transition from coarse to high resolution thus preserving far-field resolution and eliminating the corresponding drawback of grid-stretching techniques (Rahimi et al., 2019; Wu et al., 2017). In such techniques, which are extensively used in VR configurations (Abiodun et al., 2008; Fox-Rabinovitz et al., 2006; McGregor & Dix 2008; Tomita, 2008), a gradually coarsening mesh as going away from the refined region degrades the representation of large-scale circulations, because the degrees-of-freedom is held constant while decreasing the horizontal resolution away from the refined region. Whereas in VR-CESM, degrees-of-freedom are added to make a statically-refined region (Zarzycki, Levy, et al., 2014), increasing the accuracy at the far-field.

2.1.1 Grids

VR grids used in this study were developed employing the C++ based open-source software package SQuadGen (Guba et al., 2014; Ullrich, 2014). These are cubed-sphere grids consisting of quadrilateral unstructured meshes obtained by gnomic equal-angle projection of an inscribed cube onto a sphere (Dennis et al., 2012). Although the CESM framework allows use of grids with different resolutions for the atmosphere and land components depending on the scientific purpose, here, identical grids are used which allow better simulation of terrain-associated climatic features.

For our control simulation, we use the quasi-uniform 1° spectral element grid which is obtained by dividing each cube face into 30x30 spectral elements. Hereafter, this grid is denoted as ne30, referring to the number of elements along the edge of a cubed-sphere face. We employ two VR grids. The grid with the highest resolution of 0.25° (~28 km) over the study domain (Figure 1a) has a 1° base resolution and a transition zone of 0.5° in between the high and coarse resolutions. This set up takes into account the spatial spin up of transiting flows (Matte et al.,

2017) which is necessary for the development of small scale features from the low-resolution driving lateral boundary conditions as permitted by the finer resolution. The other grid with the highest resolution of 0.125° (Figure 1b) also has the same 1° base resolution, but includes two transition zones of 0.5° and 0.25°. These two VR grids are labeled as ne30x4 and ne30x8, respectively, following the same nomenclature as above. The highest resolution domains of the VR grids have an approximate latitudinal extent of 23°-59°N and longitudinal extent of 10°W-56.5°E. These three grids consist of 5400, 10212, and 20688 spectral elements, respectively. As a reference, a 0.125° quasi-uniform spectral element grid would consist of 86400 spectral elements – more than a factor of 4 as large as our finest VR grid. Throughout this study, the analysis domain is defined as the interior-most area with the highest resolution of VR grids.

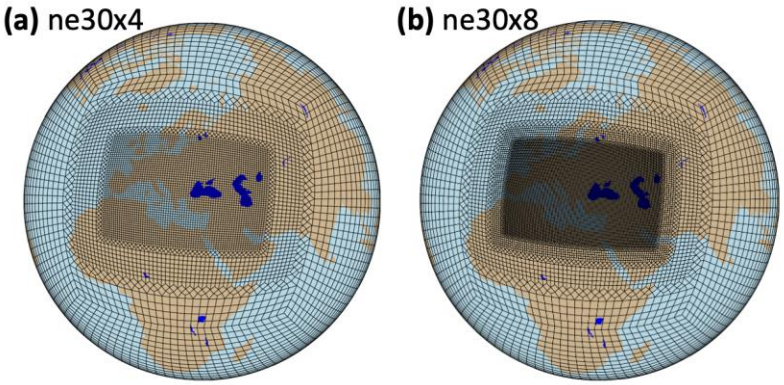

Figure 1. Variable resolution cubed-sphere grids. (a) Grid which has 1° base resolution with the highest resolution of 0.25° over the Euro-Mediterranean region (ne30x4). (b) As in (a) but with the highest resolution of 0.125° over the domain (ne30x8). Notice how the grid transition is done gradually.

2.1.2 Domain of Interest and Topographical Representation

The notable geographical features of the study domain are provided in Figure 2a, which depicts the real topography of the region at a resolution of 30 arc-seconds (~1 km) from the US Geological Survey (USGS; Danielson & Gesch, 2011) dataset – which was updated to include more accurate elevations of Greenland and Antarctica (Wijngaard et al., 2023) – using NSF NCAR's global model topography generation software package (Lauritzen et al., 2015). Figures 2b, 2c, and 2d show the representation of this topography in the three model resolutions.

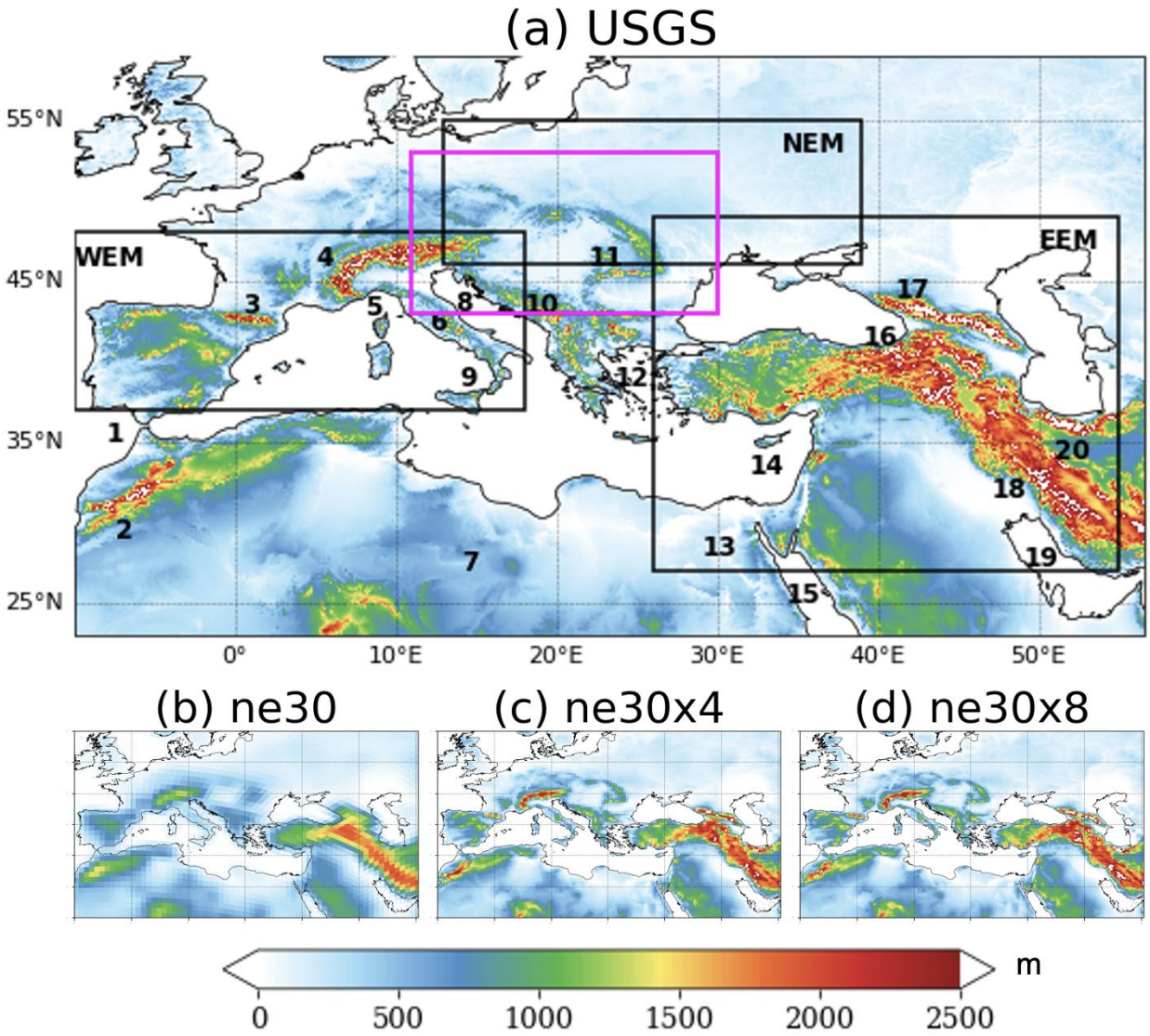

Figure 2. Representation of land topography in (a) the USGS dataset, (b) ne30, (c) ne30x4, and (d) ne30x8 grids. Model topographies are plotted on their respective native grids. The map in (a) also shows the most relevant geographical features of the Euro-Mediterranean region. The numbers denote the following features of the region: 1. Strait of Gibraltar; 2. Atlas Mountains; 3. Pyrenees; 4. European Alps; 5. Gulf of Genoa; 6. Apennines; 7. Sahara Desert; 8. Adriatic Sea; 9. Tyrrhenian Sea; 10. Dinaric Alps; 11. Carpathians; 12. Aegean Sea; 13. Nile River; 14. Levantine Basin; 15. Red Sea; 16. Kackar Mountains; 17. Caucasus Mountains; 18. Zagros Mountains; 19. Persian Gulf; 20. Alborz Mountains. Subregions denoted with black boxes in (a) and abbreviations at their upper corners, and the one denoted with a magenta box are used for subregional analyses in this work. Here, WEM, NEM, and EEM denote western, northern, and eastern Euro-Mediterranean, respectively.

Quasi-uniform 1° resolution uses a rather smooth topography (Figure 2b) to maintain numerical stability and prevent numerical artifacts, a requirement at relatively coarse resolutions (Zarzycki et al., 2015). As such, it can neither resolve the rapidly varying features nor faithfully represent the topographic details such as mountain peaks of the Euro-Mediterranean region.

Impacts of smoothing are particularly evident in the representation of maximum elevation areas. In ne30x4, the 0.25° resolution substantially improves the representation of the details of the regional topography with many topographic features and their elevations closely matching those of the USGS dataset (Figure 2c). Increasing the regional resolution further to 0.125° in ne30x8 does not seem leading to obvious additional improvements (Figure 2d) and it is quite similar to that of 0.25°.

2.1.3 Experimental Setup

Four sets of simulations were performed for this study as summarized in Table 1. The first set uses the quasi-uniform 1° grid where each element is divided in 3x3 (pg3) quasi-uniform resolution physics columns (Herrington et al., 2019) and it is referred to as ne30-n with "n" indicating that no parameter tuning is applied to the default ones in the base code. The second set of simulations uses the ne30x4 grid, again with no parameter tunings. This set is labeled as ne30x4-n. The third set, ne30x4-t, uses the ne30x4 grid, but some parameters are tuned as discussed below. The fourth set employs our highest resolution grid with the same tunings as in the ne30x4-t simulations. This set is referred to as ne30x8-t. The physics timesteps are reduced with finer resolutions which proportionally determines the other timesteps used. Throughout the manuscript "coarsest / finest (highest-resolution) simulation" will be used interchangeably with "ne30-n / ne30x8-t".

Table 1

Model Simulations

Configuration name	**Grid resolution**	**Ensemble size**	**Physics timesteps (s)**	**Number of cores/ Simulation cost***	**Modifications from the base code**
ne30-n	Quasi-uniform 1°	7	1800	1800 / 2,306	-
ne30x4-n	1°→ 0.25°	7	450	3600 / 14,224	-
ne30x4-t	1°→ 0.25°	7	450	3600 / 14,224	Tuning
ne30x8-t	1°→ 0.125°	1	225	4320 / 48,689	Tuning – updated topography source data

Note. *Simulation cost is given in core-hours per simulation year.

All the simulations are performed for the 1998-2014 period. The first 2 years of data are discarded as spin-up. Thus, we analyze monthly and daily output fields for the 2000-2014 period, a length deemed long enough to provide a representative climate of the region, including its internal variability. We ran 7 ensemble members for ne30-n, ne30x4-n, and ne30x4-t where the ensemble spread is achieved by round-off level perturbations of the atmospheric potential temperature field at initialization. However, due to its high computational cost, we ran just one member for ne30x8-t.

2.1.4 Parameter Tuning

Default CAM physics parametrizations are developed for use in coarse resolutions of order 1°. Because the default parametrizations in CESM / CAM might not be appropriate for higher resolutions with lower time steps as we use in our study, some time-stepping errors are

likely to be seen. Thus, we might expect better simulation of the climate by properly tuning related parametrizations.

Climate models involve many parameters which are tunable, that is, which are not strongly constrained by process-level observations or theory (Schmidt et al., 2017) and are subject to uncertainty. In this study, we modify four radiative tuning parameters (see below) targeting those which largely impact energy budget through their effects on the simulation of radiation, and compare the results with the non-tuned version of VR-CESM. Increasing the horizontal resolution is likely to cause deficiencies in the representation of clouds via effects on the resolved-scale boundary layer properties (Xie, S. et al., 2018). Indeed, regional top of atmosphere (TOA) longwave and shortwave cloud forcing biases worsen in 0.25° simulations compared to those with 1° (e.g., from ne30-n to ne30x4-n) (see Figures 14 and 15). The shortwave cloud forcing (SWCF) is the net solar flux (FSNT) minus the clearsky net solar flux (FSNTC) at top of the model. Similarly, the longwave cloud forcing (LWCF) is the clearsky net longwave flux (FLNTC) minus net longwave flux (FLNT) at top of the model. When positive (negative), SWCF and LWCF indicate that the clouds have a warming (cooling) effect. Specifically, low-level clouds (e.g., shallow cumulus and stratiform clouds) largely modulate SWCF by reflecting incoming solar radiation, and high-level clouds (e.g., cirrus clouds) modulate LWCF by influencing the amount of outgoing longwave radiation. Therefore, low/high clouds have a negative/positive effect on the Earth's radiative balance. By modifying those tunable parameters, we target a better agreement with observations for LWCF and SWCF, addressing the degradation caused by increasing resolution.

Table 2

Physics Parameterization Modifications in the Tuned Simulations

Parameter	**Description**	**Component / Scheme**	**Non-Tuned value**	**Tuned value**
clubb_c11b	High skewness of buoyancy damping for the third moment of vertical velocity	CAM / CLUBB macrophysics	0.35	0.375
micro_mg_dcs	Auto-conversion size threshold from cloud ice to snow	CAM / MG2 microphysics	500×10^{-6} m	1000×10^{-6} m
r_snw	Base snow grain radius	CICE / Delta-Eddington	1.25 standard deviations	1.50 standard deviations
dt_mlt	Snow melt onset temperature	CICE / Delta-Eddington	1.5 °C	1.0 °C

Among several tunable parameters, we choose the ones listed in Table 2, following Wijngaard et al. (2023) as the parameters which have a major influence on the cloud formation. First, to increase low-level cloudiness, we increased the damping on vertical velocity skewness in CLUBB (clubb_c11b). clubb_c11b is one of the most impactful parameters for shallow convection and thus for the formation of low clouds (Guo et al., 2015). Increasing its value favors LWCF by damping buoyancy velocities, which reduces the vertical skewness of cloud distribution and consequently increases the fraction of low clouds.

Second, to thicken high clouds, microphysical auto-conversion size threshold for ice to snow (micro_mg_dcs) was increased. micro_mg_dcs is a MG2 microphysics parameter specifying the threshold for a cloud ice particle must grow before it is converted to snow. Larger values of this parameter mean retention of larger ice particles within glaciated clouds. This reasonably leads to larger LWCF because the duration before cloud particles precipitate increases.

Finally, for the purpose of cooling the high latitudes, shortwave radiation and albedo over sea-ice and snow increased by increasing base snow grain radius (r_snw) and decreasing snow melt onset temperature (dt_mlt) in the sea ice component. These adjustments of the optical properties of snow and sea ice change the base albedos and consequently influence shortwave radiation absorbed by Earth's surface (Briegleb & Light, 2007).

With these tunings, we obtain a new 7-member ensemble (ne30x4-t). The single ne30x8-t simulation was also run with the same tunings.

2.2 Evaluation Methodology

To evaluate our simulations, various observational, reanalysis, and satellite-derived datasets are used as summarized in Table 3. These datasets are generally preferred for their relatively high spatial and temporal resolutions.

Table 3

Summary of the Datasets Used in This Study

Dataset	**Spatial / Temporal resolution**	**Field used in the analysis**	**Source and reference**
CRU TS v. 4.05	0.5°x0.5° (All land areas (excluding Antarctica) / Monthly	2m Temperature (T2m), Precipitation	Climatic Research Unit (Harris et al., 2014; Harris et al., 2020)
CPC	0.5°x0.5° / Daily	Daily max temperature and precipitation rate	NOAA Climate Prediction Center (Chen et al., 2008; Xie, P. et al., 2007)
E-OBS v. 27.0e	0.25°x0.25° / Daily	Daily precipitation rate	European Climate Assessment & Dataset initiative (Cornes et al., 2018)
ERA5	0.25° x 0.25° (37 pressure levels) / Monthly	Horizontal winds, vertical wind velocity, relative humidity, specific humidity, snow depth	European Centre for Medium-Range Weather Forecasts (ECMWF) (Hersbach et al., 2020)
CERES EBAF v.4.2	1°x1° / Monthly	Shortwave and longwave cloud radiative forcing (SWCF and LWCF)	NASA (Kato et al., 2018; Loeb et al., 2017)
AMSR2	0.25° x 0.25° / Monthly	Column integrated water vapor	Japan Aerospace Exploration Agency (JAXA) (Wentz et al., 2014)

We evaluate the climatological performance of simulations with respect to T2m and precipitation using Climatic Research Unit gridded Time Series (CRU TS v.4.05) monthly data. CRU TS dataset is constructed by interpolation of monthly climate anomalies from meteorological stations across the land areas excluding Antarctica. For daily maximum T2m, NOAA Climate Prediction Center (CPC) dataset is utilized. CPC daily data and the European Climate Assessment & Dataset initiative (E-OBS) data are used for daily precipitation rate. E-OBS data cover Europe and Northern Africa. The fifth generation European Center for Medium-range Weather Forecast (ECMWF) atmospheric reanalysis (ERA5) data at single and pressure levels, combining past observations with models using data assimilation techniques, are used for performance analysis of fields such as horizontal and vertical winds, relative humidity, specific humidity, and snow depth and for quantities calculated by using these fields such as the vertically-integrated vapor transport (IVT). The Clouds and the Earth's Radiant Energy System (CERES) Energy Balanced and Filled (EBAF) dataset is used to evaluate shortwave and longwave cloud forcings. The Advanced Microwave Scanning Radiometer 2 (AMSR2) microwave satellite data are used in comparisons for column integrated water vapor.

We use root-mean-square-error (RMSE), which is the root of the mean of the squared errors between the simulated and observed values, and relative root-mean-square-error (rRMSE), which quantifies the model performance relative to observations as percentages to evaluate our simulations. While RMSE has the same unit as the field being evaluated, rRMSE is a dimensionless measure. In the evaluation of the total precipitation rate, grid points receiving less than 1 mm/d annual precipitation are excluded from the calculations of rRMSE to avoid exaggeration of biases and to better interpret the influence of increased resolution. Scale-dependent skill of the simulations is quantified via pattern correlation coefficients between the simulations and observations. Significance of differences between simulated and observed values is assessed employing a two-tailed Student's t-test with a p-value of 0.05. Given that the model output data both on land and ocean, whereas, the observational dataset, CRU, provides data over land only, to compare the areal means of T2m and precipitation from the simulations with that of observation over land, model data are masked based on Natural Earth's land shapefile at 1:10m scale (https://www.naturalearthdata.com/, (accessed on 9 October 2023)).

To enable direct comparisons of simulated fields with those of the above observational and reanalysis datasets, model output files were regridded onto the respective regular longitude-latitude grids of the datasets. For this purpose, we employ a first-order conservative mapping procedure from the Earth System Modeling Framework (ESMF) library. This is a method which preserves the integral, i.e., conservation, of the source field across regridding and supports regridding between unstructured and structured grids. Because CAM6 uses hybrid pressure coordinates in the vertical, we also perform logarithmic vertical interpolation to the respective level coordinates of the evaluation datasets when necessary.

For long-term climatological analysis, we use ensemble means of ne30-n, ne30x4-n, and ne30x4-t simulations and the single member of ne30x8-t simulation. When analyzing climate extremes for precipitation over sub-regions, we check whether this single member lies within the ensemble spread of other simulations by using all members of the ensembles.

3 Results and Discussion

In this section, simulation results are compared with observations and reanalysis products. Subsections 3.1 and 3.2 are devoted to precipitation and T2m, respectively. Subsection 3.3 documents the representation of extreme daily maximum temperature and precipitation. Effects of parameter tuning are discussed in subsection 3.4.

3.1 Precipitation

Simulation of precipitation is challenging, largely because it depends on small-scale processes that need to be parametrized. Parametrization leads to uncertainties such as those related to the cloud processes. For regions with high spatial heterogeneity, like our study domain, interactions with the surface features (e.g., orography, coastlines, and land–sea contrasts) add much more complexity (Flato et al., 2013). This difficulty is present for the interpretation of results as well. Because so many scales are interacting with each other, sources of errors should be understood well to avoid misinterpretations (Di Luca et al., 2021).

For precipitation, unless the resolution is increased to more than that of deep-convection-permitting scales (i.e., < 4 km) in order to mostly eliminate the parameter dependency, added value of increased resolution is limited to certain regions such as those with sharp topographic contrasts (e.g., near high elevation terrain and coastlines). The effect of higher spatial resolution

is not expected to be seen distinctively for processes occurring at scales that can already be resolved by coarser resolutions over homogenous terrain. Moreover, increasing resolution many times leads to increased biases because the model parameterizations are often tuned for coarse, operational resolutions as discussed above.

With these caveats, overall, all simulations produce the spatial variability of regional total precipitation in good agreement with observations with relatively high pattern correlations between 0.87-0.95 (Figure 3 and Figure S1). We see high precipitation in the northwest of the study domain, particularly over windward sides of mountain ridges, and at the west coasts, and low precipitation in the south (Northern Africa and Arabian Peninsula). The correlations for VR simulations are typically higher than that of the coarse control simulation.

For quasi-uniform 1° control simulation, the largest/smallest biases are seen in JJA/MAM (rRMSE values for ne30-n are 39.7, 29.5, 173.9, and 69.9% for DJF, MAM, JJA, and SON, respectively) (Figure 3). The amplitudes of wet/dry biases over the windward/leeward sides of the high mountains and the dry biases over the coasts exceed 2 mm/d in some seasons and regions (e.g., wet/dry bias on the windward/leeward side of European Alps in DJF/MAM and dry bias in the east coast of Black Sea in JJA). Increasing resolution from 1° to 0.25° (compare the columns corresponding to ne30-n and ne30x4-n simulations, respectively) improves the model performance annually and seasonally (rRMSE values for ne30x4-n are 34.6, 23.6, 133.1, and 50.3% for DJF, MAM, JJA, and SON, respectively). The wet/dry biases over the windward/leeward sides of the high mountains and dry biases at the western coasts substantially reduce with increased resolution. Parameter tuning (i.e., from ne30x4-n to ne30x4-t) degrades model performance for JJA, largely because of the expansion of the higher magnitude dry biased area over the eastern Europe, whereas it leads to improvements in other seasons (rRMSE values for ne30x4-t are 33.8, 23.3, 154.8, and 50.1% for DJF, MAM, JJA, and SON, respectively). Further increasing the resolution (i.e., from ne30x4-t to ne30x8-t) overcomes this degradation in JJA to some extent but leads to slightly larger biases than that of ne30x4-t in other seasons (rRMSE values for ne30x8-t are 34.7, 26.6, 138.5, and 57.4% for DJF, MAM, JJA, and SON, respectively). The improvement in JJA shows that, the highest resolution simulation (ne30x8-t) is able to resolve more smaller scale processes related to convective activity which dominates summer precipitation and it leads to an apparent improvement despite the degradation (as seen in other seasons) related to lack of extra parameter tunings.

The precipitation bias contrast on the windward/leeward sides of high mountains, which can exceed ~7 mm/d in places for ne30-n, is reduced with increased resolution as a demonstration of added value of VR-CESM. It is a manifestation of improved orography which better resolves adjacent topographical gradients (i.e., sharp topographical contrasts) leading to better simulation of moisture convergence. Another added value of increased resolution is seen on the coastlines. The biases seen for ne30-n over the western coasts (e.g., dry biases over the west coasts of Iberian Peninsula in MAM and SON; northwestern coast of Africa in DJF, MAM and SON; southwest coast of Türkiye in DJF; and easternmost coast of the Mediterranean Sea in DJF) diminishes with increased resolution. An explanation for these reductions in coastal biases will be discussed later.

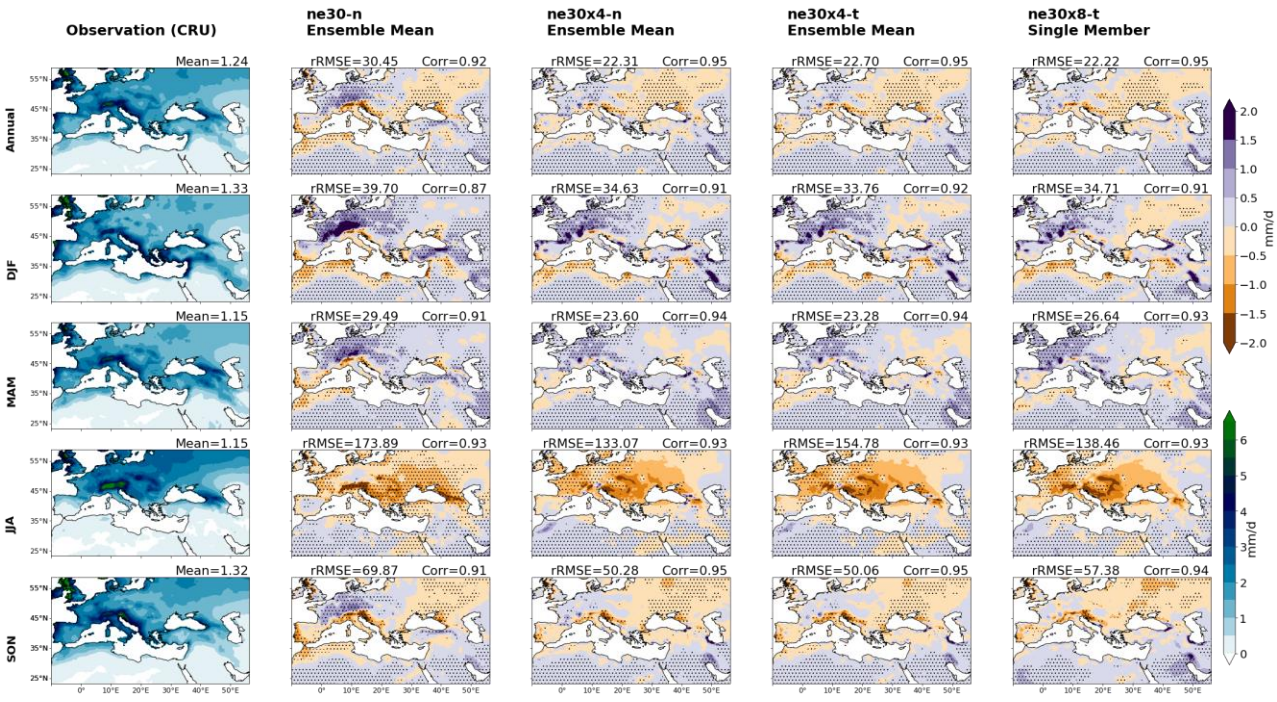

Figure 3. Observational annual- and seasonal-mean (rows) distributions (first column) and model (ne30-n, ne30x4-n, ne30x4-t, and ne30x8-t in order) minus observations annual and seasonal difference distributions for precipitation (other columns). The observations are from CRU. Relative root-mean-square-errors (rRMSE) and pattern correlations as well as the areal means for observations are given at the top of each panel. rRMSE is calculated for the grids with annual precipitation more than 1 mm/d. The dots indicate areas where the differences are statistically significant at the 95% level based on two-sided Student t-test. The observations and difference distributions use the lower and upper color bars, respectively.

Some persistent precipitation biases remain at all resolutions. For example, in summer, a warm and dry bias over the Central-Eastern Europe exists in all simulations (Figures 3 and 9). To investigate reasons for this persistent bias, we study the relationship between T2m and precipitation over the region shown in magenta in Figure 2a. We show the annual cycles of T2m and precipitation biases and their time series in Figure 4. For all simulations, there exists a statistically significant (with a p-value of 1.3×10^{-5} or smaller) strong anti-correlation (with an amplitude of 0.60 or more) between these two biases (Figure 4 – right) indicating a causal relationship between these two surface variables over this region. The peaks of the precipitation deficit occur almost at the same time (in July) for all resolutions. The temperature excess peaks in August/September for VRCESM/quasi-uniform 1° simulations respectively and precipitation deficit precedes the temperature excess in this respect (Figure 4 – left).

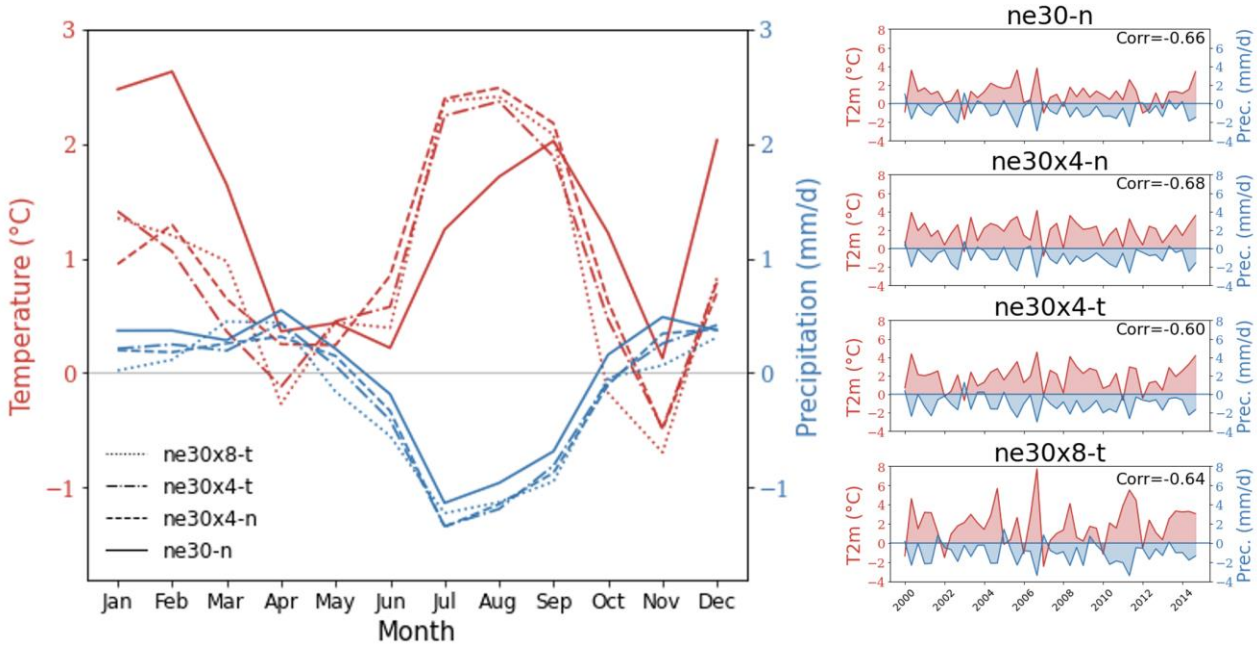

Figure 4. Anti-correlation between precipitation and T2m in summer for the analysis region shown with a magenta box in Figure 2a. Left: Annual cycles of temperature (red) and precipitation (blue) biases; right: Time series of biases of temperature (red) and precipitation (blue). In the time series plots, the correlation coefficients are provided at the upper right corner of each panel.

The warm bias over the region can be attributed to the land-atmosphere interactions following the precipitation deficit. The time lag between precipitation deficit and temperature excess is consistent with development of related mechanisms. The mechanism, as proposed by several studies (e.g., Lin et al. 2017; Vautard et al., 2007), should be working as follows: Precipitation deficit leads to soil moisture deficit which results in less evaporative cooling and ultimately higher temperatures. Underestimation of precipitation rates in simulations can be explained by less moisture transport due to the drier climate. As a further feedback, evaporative demand over land causes less cloud development and precipitation leading to further surface warming (Tuel & Eltahir, 2021).

A large wet bias is evident over the western Europe except in JJA with its highest magnitude occurring during winter months (DJF), when this region experiences its largest precipitation, and on the windward side of the European Alps. This bias largely diminishes with high resolution. Over the western Mediterranean land areas, the North Atlantic Ocean is the major moisture source especially in winter (Batıbeniz et al., 2020). Therefore, we investigate the mechanism behind this winter wet bias considering the large-scale dynamics of the atmospheric circulation. For this analysis, we employ ERA5 reanalysis data for evaluation of the model solutions because ERA5 provides all the needed fields, i.e., relative humidity and horizontal winds at pressure levels as well as the calculated IVT at relatively high horizontal and vertical resolutions (0.25°x0.25° and 37 pressure levels, respectively).

We present model minus ERA5 difference distributions for IVT, 850-hPa wind vectors, and relative humidity for winter (DJF) in Figure 5. Both coarse and high-resolution simulations show positive IVT differences directed towards the western Europe at mid latitudes. IVT biases

exceed 60 kg $m^{-1}s^{-1}$ for ne30-n and 20 kg $m^{-1}s^{-1}$ for VR simulations (Figure 5 - left). It is clearly seen that 850 hPa westerly wind difference vectors carry North Atlantic moisture right over the wet-biased area in the Northwestern Europe in all simulations (Figure 5 - right). Strength and orientation of wind difference vectors and vapor transport are consistent with the magnitude of wet bias for different resolutions. Over the area with stronger moisture transport, relative humidity is also higher in the simulations. Overestimation of relative humidity reaches to more than 20% for ne30-n, 12% for ne30x4-n and ne30x4-t, and 8% for ne30x8-t. There is a notable reduction in relative humidity with increasing resolution which is also discussed in Herrington and Reed (2017). Therefore, the wet bias can be attributed to the larger precipitation produced by stronger wind difference vectors with a direction in favor of carrying moisture over the wet-biased area, together with higher relative humidity. The improvement in this bias with higher resolution is related to better representation of water vapor transport from the North Atlantic at these resolutions.

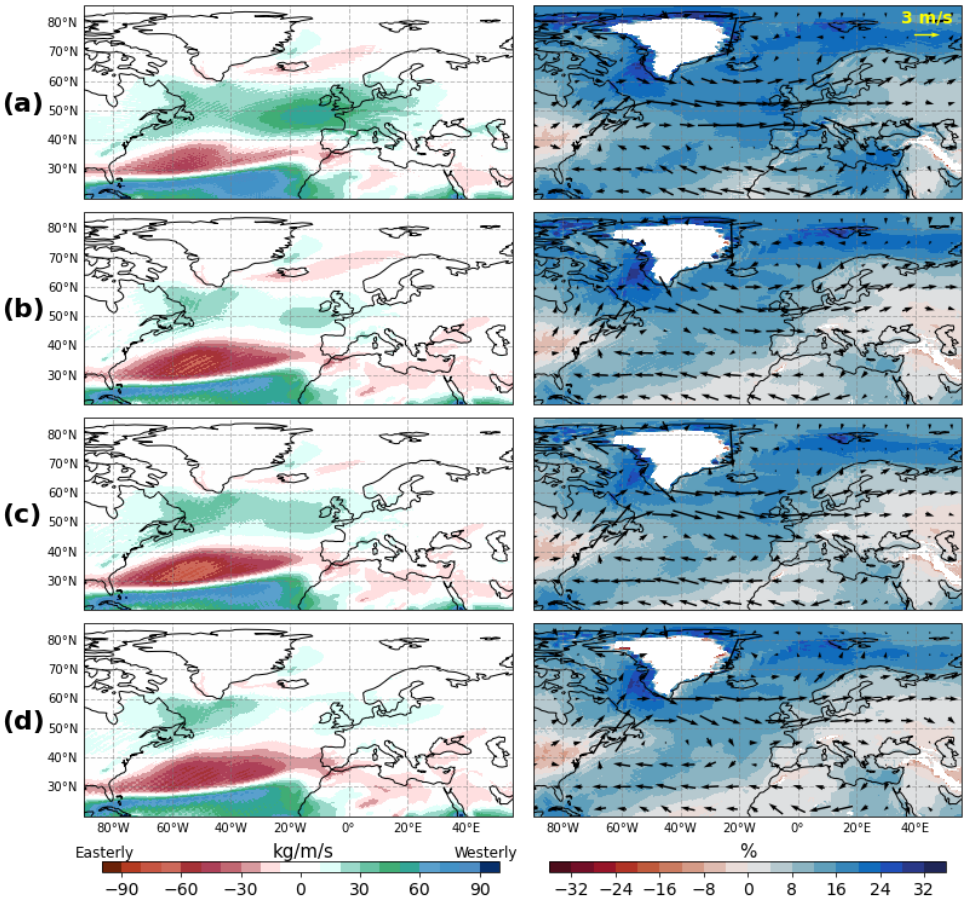

Figure 5. Differences (simulations-ERA5) of vertically-integrated vapor transport (IVT) (left), and 850 hPa winds (vectors) and relative humidity (right) for DJF; a) ne30-n, b) ne30x4-n, c) ne30x4-t, and d) ne30x8-t.

The orientation and strength of the 850 hPa wind differences can be explained by geopotential height differences at 500 hPa, the level which is commonly used to investigate the large-scale circulation. Figure S2 shows the differences of 500 hPa geopotential height between VR simulations and the control simulation for DJF. There is a positive height difference between

the VR simulations and control simulation over the North Atlantic stretching into the North-Western Europe which is indicative of more cyclonic flow represented by the control simulation. Cyclonic activity orients moist air onto Western Europe. The negative sea level pressure bias over this region is also consistent with the higher intensity of low-pressure systems. This is a demonstration of the ability of VR-CESM in resolving dynamical processes driving precipitation along with its better topography treatment.

To highlight the role of orography in contributing to the precipitation rates in these simulations, we evaluate longitudinal distributions of precipitation within the latitude band between 44°N and 48°N which includes the European Alps. Figure 6 shows the elevation, precipitation, and vertical pressure velocity averaged along this latitude band for DJF – chosen for being the season when the advection of moisture from the North Atlantic is most prominent. Elevation is plotted for the three different grids (ne30, ne30x4, and ne30x8) used in the simulations and for the USGS dataset.

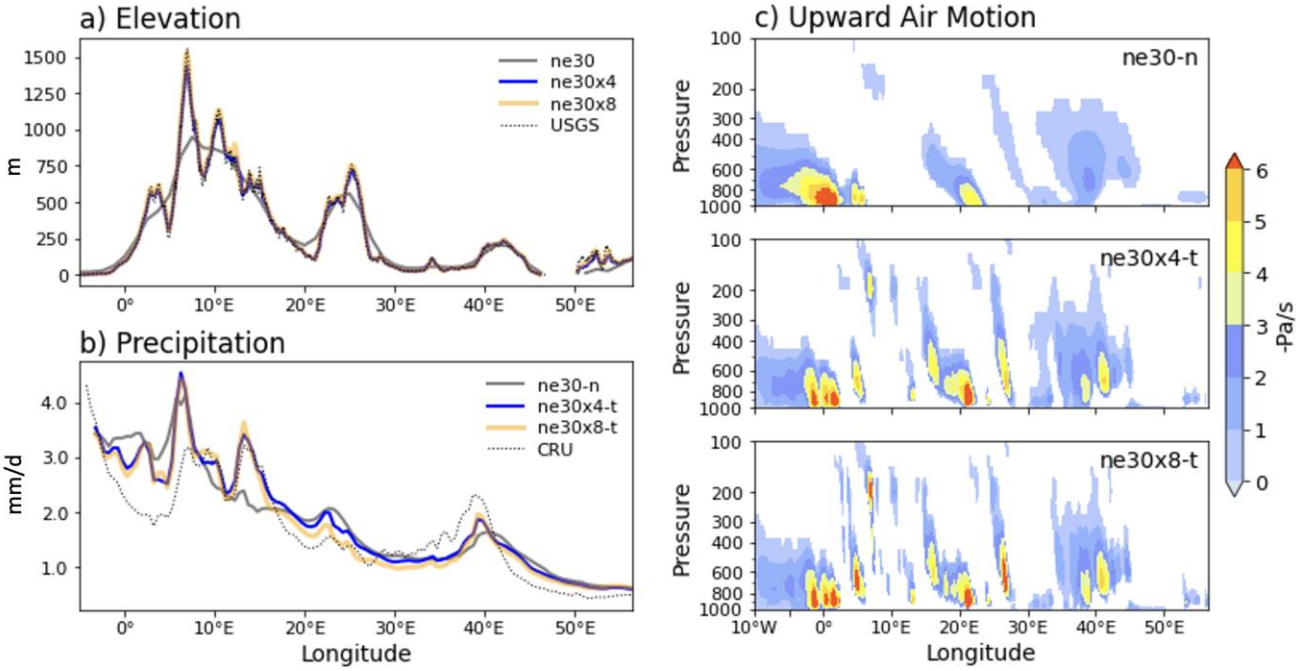

Figure 6. Longitudinal distribution of (a) terrain height, winter (b) precipitation rate and (c) vertical pressure velocity corresponding to upward motions (scaled with a factor of 100 and multiplied by -1) averaged over the latitude range of 44°- 48°N.

In simulations, the persistent wet bias over the northwest of the study domain during winter is clearly present across the windward side of the European Alps (~ 3°W-7°E). This wet bias is highest for ne30-n (up to more than ~1.5 mm/d). All simulations reach a maximum in precipitation at ~7°E at about 4.5 mm/d which then rapidly declines to the east. For ne30-n, this maximum precipitation rate is smaller than that of the VR simulations due to its smoother topography. The simulated maximum occurs a bit to the west compared to observations as a result of differences in the representation of elevation. ne30-n underestimates precipitation at the lee side (~ 8°-16°E). We see the typical dry bias over the Eastern Europe (~ 34°E-41°E and ~ 30°E-41°E for control and VR simulations respectively) which reaches ~0.6 mm/d (see also Figure 3). The precipitation rates for ne30x4 and ne30x8 are quite similar as a reflection of their

similar topographical representations. As shown in Figure 6c, the locations and expansions of upward air motions represented by vertical pressure velocities better coincide with the respective terrain upslopes and downslopes in VR-CESM high-resolution simulations. Orographically forced upward motions are strongest and most vertically expanded for ne30x8-t.

Reasonably, increased resolution might be expected to better resolve the convective precipitation due to its ability to represent smaller scales at which convection takes place. However, it is not the case for our simulations. Figure 7 shows the distribution of the fraction of convective precipitation (i.e., the percentage of total precipitation contributed by convective precipitation) for the simulations, annually and seasonally. In the region, maximum and minimum convective precipitation fraction are seen in JJA and DJF, respectively, in all simulations. It appears that while convective precipitation fraction decreases, large-scale precipitation fraction increases with increased resolution. The coarsest and finest resolution simulations produce the highest and lowest fraction of convective precipitation, respectively, in all seasons. For instance, JJA fractions are 43.2 and 15.0% and DJF fractions are 18.0 and 6.3%, respectively. In summertime, for the coarsest resolution, fraction of convective precipitation is very high (more than 75%) over most of the southern Europe, Anatolia, and east coast of the Black Sea, and it exceeds 45% over the rest of Europe and southwest Russia, Arabian Peninsula, and northwest of Africa. For the highest resolution, relatively higher fractions (35-65%) are confined to the coastal regions. The highest fractions are located over land in summer and they shift to over sea as the seasons progress.

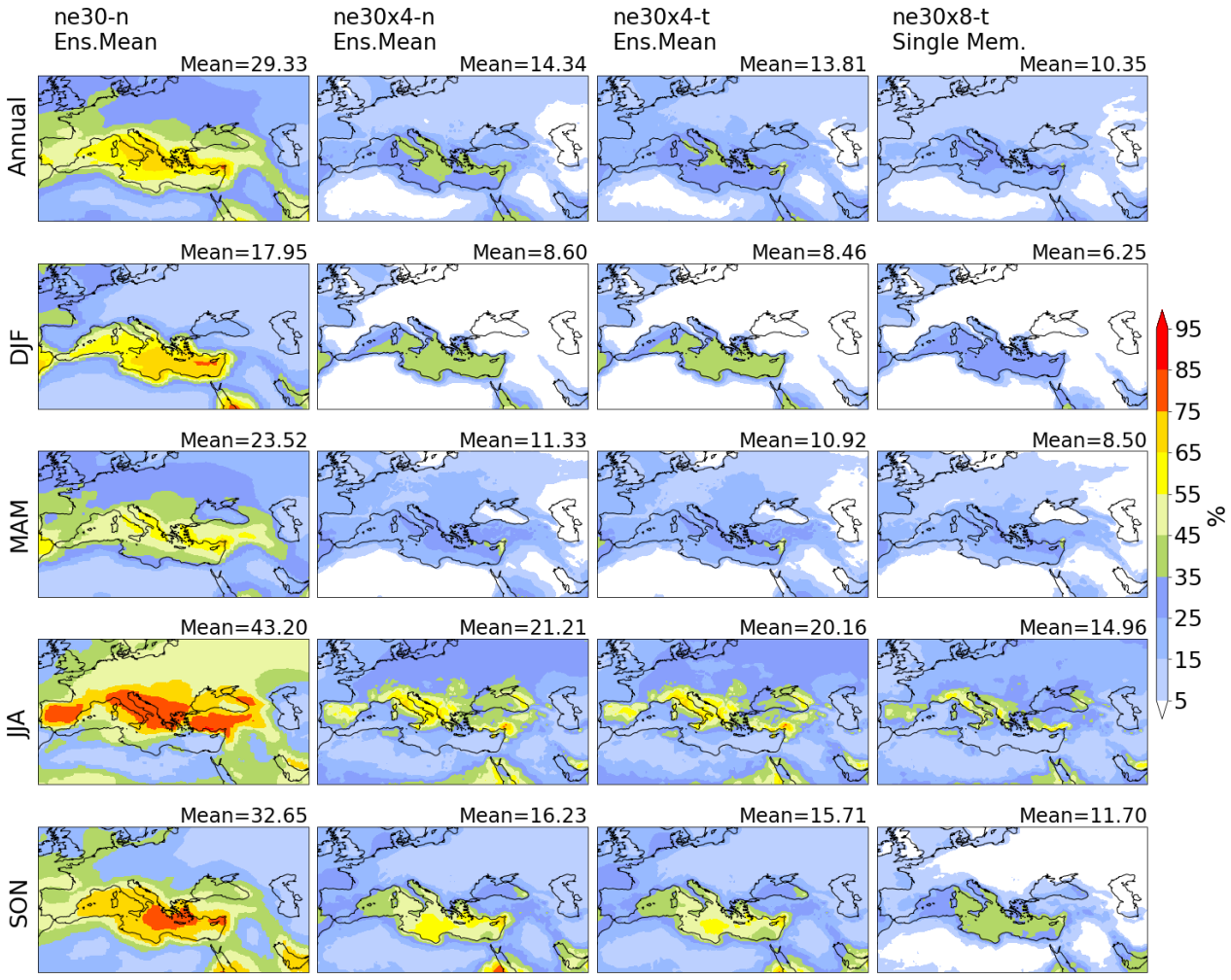

Figure 7. Annual- and seasonal-mean distributions of the fraction of convective precipitation. Areal means (as percentages) are given at the upper right of each panel.

The shift in the partitioning of convective and stratiform precipitation is a known phenomenon for CAM and for other atmospheric models as well. Consistently, in our simulations, the ratio of annual large-scale (stratiform) to total precipitation rate is lowest/highest and the ratio of convective to total precipitation rate is highest/lowest for the coarsest/finest simulation (Figure 8). This shift can be explained by the sensitivity of parametrized convective and stratiform precipitation rates to resolution following the causality set forth by Herrington and Reed (2020). In effect, the larger resolved upward vertical velocities supported at higher resolutions increasingly compete with the convection scheme to stabilize the atmosphere. These larger velocities facilitate subsidence as a consequence of mass conservation, which tends to dry out and stabilize the atmosphere further. The reduction in physics time-step also contributes to the reduction in convection scheme activity (Williamson, 2013).

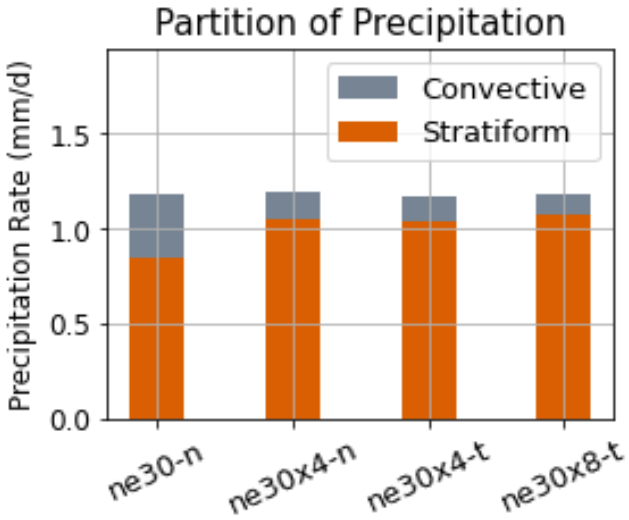

Figure 8. Partitioning of stratiform and convective precipitations in simulations.

As an indicator of this progressive drying of atmosphere with increasing resolution, area weighted regional averages of simulated total (vertically integrated) precipitable water decreases with increasing resolution in our model results (15.69, 15.09, 15.26, and 15.06 kg/m^2 respectively for 1°, 1/4° (non-tuned and tuned), and 1/8°). Figure S3 shows differences of high-resolution simulations (ne30x4-n, ne30x4-t and ne30x8-t) from ne30-n for total precipitable water (TMQ). We note that ne30x8-t has the highest magnitude of differences and the negative differences follow the topography (e.g., the biggest and the smallest negative differences exist over the highest and the lowest elevations, respectively).

3.2 2-Meter Temperature (T2m)

Overall, all simulations are able to represent the spatial variability of T2m well with pattern correlations between 0.95-0.99 over the refined domain in all seasons (Figure 9 and Figure S4). The lowest (but still quite high) pattern correlations are seen in JJA. VR simulations have slightly higher correlations relative to ne30-n in all seasons. From a qualitative standpoint, existence of similar distribution patterns with quasi-uniform coarse resolution shows that variable resolution simulations produce credible climatic representations in terms of temperature.

Based on the regional averages, the coarsest and the finest resolutions tend to overestimate and underestimate, respectively, average T2m compared to observations both annually and seasonally (except a slight overestimation by the finest resolution in JJA). For example, the winter-mean T2m is 4.59, 5.22, and 4.35°C in CRU, ne30-n, and ne30x8-t, respectively, with the largest relative gap seen in winter (Figure S4). This finding can be partly attributed to the overestimation of T2m over mountainous regions in ne30-n due to its smooth topography and smaller overestimation or underestimation of T2m in ne30x8-t. It should be noted, however, that warm bias of CRU as a consequence of the scarcity of stations over mountainous regions can artificially contribute to the cold bias of high-resolution simulations (Giorgi et al., 2004). Also, a supporting explanation might be related to simulated and observed snow-ice albedo feedbacks. Because less snow leads to increased temperatures by absorbing more shortwave radiation, underestimation/overestimation of snow cover in ne30-n/ne30x8-t

(Figure S5) over high mountains might be contributing to higher/lower temperatures. As an indicator of less accurate representation of topographical heights, ne30-n shows a dry snow water equivalent bias at high elevations. For VR simulations, the snow bias over mountains, which worsens with elevation, could also be a result of incorrect lapse rates, because CESM has not been developed for small grid spacings such as ours (Rhoades et al., 2018).

There are statistically significant warm biases well exceeding 6°C over the mountains and coasts in ne30-n (Figure 9). Also, statistically significant cold biases over the southern regions exceed 5°C locally. For this coarsest simulation, DJF is the season showing the largest biases (with an RMSE of 2.4°C) and JJA is the season with the lowest pattern correlation value of 0.95. The impact of increased resolution in the representation of T2m is clearly seen in all seasons, as quantified by the RMSE values and also with a decrease in the total area with statistically significant differences from observations. For example, ne30x4-n has considerably lower RMSE values than ne30-n with higher pattern correlations (RMSE values of 1.4, 1.1, 1.7, and 1.1°C and pattern correlations of 0.99, 0.99, 0.97, and 0.99 for DJF, MAM, JJA, and SON, respectively). For ne30x4-n, JJA is the season with the largest biases and with the lowest relative improvement over ne30-n among other seasons, though still representing a considerable improvement. Parameter tuning applied to ne30x4-n yields mixed results. ne30x4-n and ne30x4-t simulations have quite similar bias patterns and equal pattern correlations in all seasons. A notable difference is seen in DJF, when RMSE value increases after tuning (from 1.38 to 1.50°C). ne30x8-t has the lowest biases in all seasons although further increasing the resolution does not result in a proportional improvement (as much as that is seen when resolution is increased to 0.25°). In this highest resolution simulation, JJA remains as the season with the largest biases as in both 0.25° simulations.

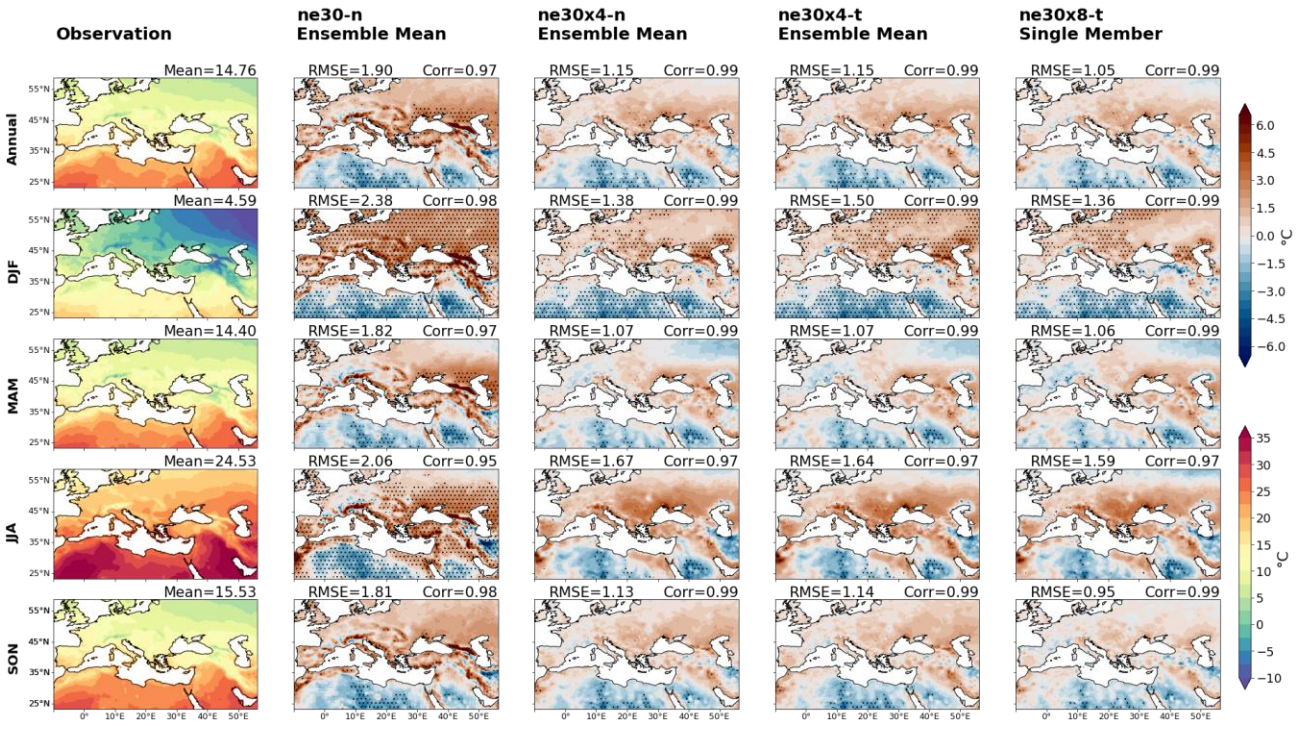

Figure 9. Same as Figure 3 but for 2-m temperature. RMSE values are given at the upper left of

difference plots. The observations and difference distributions use the lower and upper color bars, respectively.

A general warm (cold) bias is seen over the northern (southern) parts of the region, which persists in all seasons. Also, there exists a warm bias in Central-Eastern Europe which is most pronounced in summer. These two persistent biases will be discussed later. Annually, most prominent improvements are seen over high elevations such as the Atlas, Pyrenees, Alps, Apennines, Caucasus, Kackar, Alborz, and Zagros mountains and at the coasts. The warm biases over the high mountains and coasts decrease from more than 6°C to less than 2°C with increased resolution. While overestimation of temperature at high elevation terrain, which typically occurs throughout the entire year, is alleviated with higher resolution, the uncertainties of the observational data, such as a possible bias towards low-elevation stations, cannot be ruled out. Improvements are generally less pronounced in regions without strong orographic gradients highlighting the added value of higher resolution resulting from having a better topographic representation. For all configurations, typical warm biases over the west coasts and cold biases over the southwest inlands can be partly attributed to the representation of extreme hot temperatures in the simulations (Figure 11).

For analysis of the seasonal evolution of T2m, we divide the study domain as north and south of 30°N following the Intergovernmental Panel on Climate Change's (IPCC) classification of sub-regions (Iturbide et al., 2020). Over both subregions, all simulations capture the observed seasonal cycle of T2m well (Figure S6). Both subregions show maximum temperature values in summertime and minimum ones in wintertime while northern mean temperatures are consistently ~10°C lower than the southern ones all over the seasonal cycle. For all simulations, we see a small overestimation (less than ~1.5°C) during summer months (also during winter for ne30-n) over the northern part and a small underestimation (less than ~2°C) throughout the year over the southern part. These results are consistent with the spatial distribution of biases (Figure 9).

In VR simulations, summer stands out as the outlier with the highest magnitudes of biases. It is the season when small scale processes dominate and topography has a prominent influence. Therefore, we want to explore the ability of VR-CESM in representing the summer circulation features over the Euro-Mediterranean region. During this period, the circulation over the region is mainly dominated by an interplay of influences of the Azores High pressure system, South Asian monsoon, a northerly flow (e.g., the Etesians), and the highly complex topography of the region. A mechanism behind the subsidence causing hot and dry summers in the region is suggested by Rodwell and Hoskins (1996) as a monsoon-desert mechanism. This mechanism is also discussed in Simpson et al. (2015). Briefly, the subsidence in the region primarily exists due to the remote diabatic heating of the Asian monsoon which induces a Rossby-wave pattern to the west, extending into the Euro-Mediterranean region. The maxima and descent of the northerly flow, which is synchronous with the monsoon convection, favors a stronger Rossby wave effect by causing a weaker easterly jet (Tyrlis and Lelieveld, 2013). The Etesians are regional scale low-level northerly winds blowing over the Aegean Sea Basin during the extended summer from May to September (Dafka et al., 2016) with maximum persistence, intensity, and frequency during July and August. The adiabatic warming occurring as a result of the large-scale subsidence counteracted by the southward-blowing Etesian winds at the lower troposphere inhibits cloud formation and convection causing dry summers with clear skies. Interaction of the regional topography exerts a dominant influence in localizing the regions of the subsidence by inducing orographically locked summer anticyclones and in amplifying the subsidence and the

northerly flow. As it is stated in Simpson et al. (2015), about 20% of the Mediterranean summertime moisture deficit can be attributed to the mountain-induced circulation. To understand the large-scale dynamics of the atmosphere, vertical wind velocity at the upper troposphere can be a useful field to look at. It shows the areas of upward motion/ascent and downward motion/subsidence. Our simulations are able to represent the summer subsidence-ascent pattern in agreement with the monsoon-desert mechanism mentioned above, also consistent with the ERA5 data (Figure S7). There is a subsidence over our study domain which is most pronounced over the Aegean Sea and an ascent over the South Asian monsoon region. The simulations are also able to capture the subsidence regions over the eastern Mediterranean and east of the Caspian Sea located at the eastern flanks of low-level (850 hPa) orographically locked anticyclones centered over the Northwest Africa and Zagros mountains. In summer, topography exerts the greatest influence on these subsidence patterns because it is the season when the low-level incident flow is easterly (which is westerly in other seasons).

Over the southern part of the study domain (Northern Africa and Arabian Peninsula), as noted earlier, there is a general cold bias in contrast to a general warm bias in the north. This southern cold bias can also be explained with land-atmosphere interactions. Figure 10 depicts the differences of the simulations from ERA5 for latent heat flux (Figure 10a) and precipitation (Figure 10b) as well as the correlations of latent heat flux and precipitation differences (Figure 10c). Over the southern part, more precipitation (i.e. positive precipitation biases) drives more evapotranspiration. It leads to more evaporative cooling and results in a colder climate (Mueller and Seneviratne, 2014). Here, much higher proportion of the net radiation is transferred to the atmosphere by latent heat flux leading to positive latent heat flux biases (Figure 10a). Due to low rainfall rates this is a soil-moisture limited area. High positive correlations between the precipitation and latent heat differences indeed confirm the active soil moisture – latent heat flux coupling which is a characteristic of water limited regimes. Similarly, general warm biases over the north are also consistent with the underestimation of latent heat flux by all model simulations.

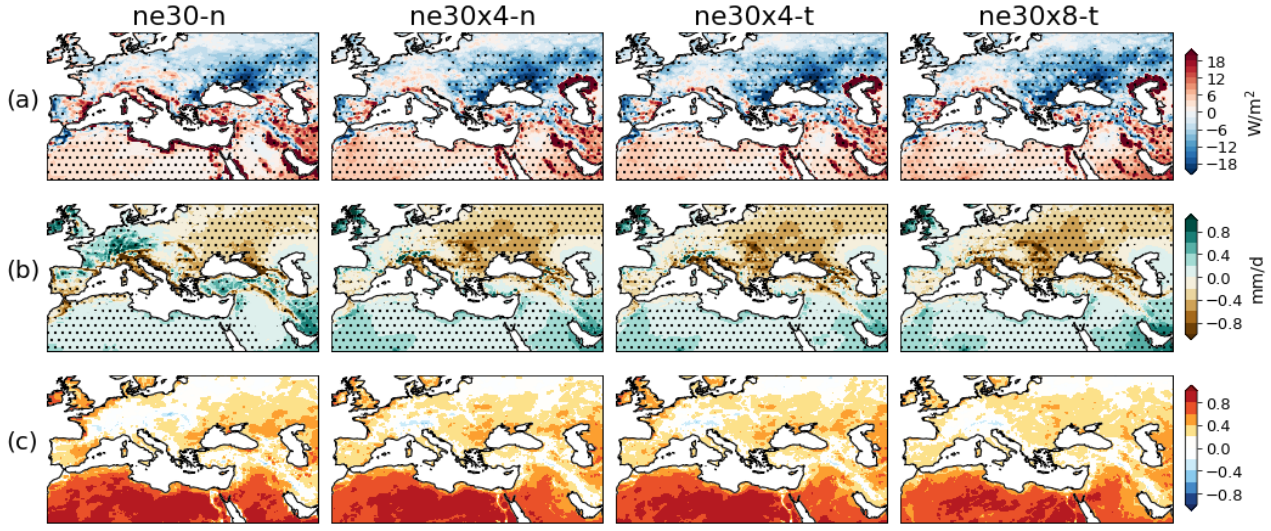

Figure 10. Annual differences of the simulations from ERA5 for (a) latent heat flux and (b) precipitation. (c) Correlations between precipitation and latent heat flux differences. Precipitation bias plots use ERA5 for consistency with the latent heat flux difference plots. The dots indicate

areas where the differences are statistically significant at the 95% level based on two-sided Student t-test.

There are large positive biases of > 20 W/m^2 for latent heat flux in ne30-n along the coasts (e.g., the coasts of the Mediterranean Sea, the Red Sea, and the Persian Gulf). These biases substantially diminish in higher resolutions. Song and Yu (2017) show that heat fluxes better capture the complex air-sea interactions near the coastal areas in high-resolution simulations where the coastlines and topography-related oceanic and atmospheric processes and their complex interactions are better represented. In high-resolution simulations, there exist large positive latent heat flux biases in the north of the Caspian Sea. This positive bias can be explained by the differences between the land masks applied to these simulations and the ERA5 land-sea mask (Figure S8). Because the Caspian Sea is handled by the land component in CESM in the ne30 runs (not by the ocean component as in the ne30x4 and ne30x8 runs) we do not see that positive bias for ne30-n.

3.3 Climate Extremes

To evaluate how climate extremes are represented at different resolutions, we consider the 99th percentile of daily precipitation and daily maximum T2m (Tmax). These are commonly used metrics for defining climate extremes and they are also important for our region. For observations, we use the CPC dataset for extreme daily temperatures and both E-OBS and CPC datasets for daily extreme precipitation. Because we do not have daily outputs for ne30x4-n, it is not included in this analysis.

3.3.1 Extreme Maximum Temperature

Figure 11 shows observational distributions of the 99th percentile of daily maximum temperatures (first column) and differences of the simulations from observations (other columns). The highest maximum temperature values occur over the south of the region (Northern Africa and Arabian Peninsula) reaching more than 45°C whereas the lowest values are over the northern and high elevation regions. In the south, although there are several overestimated coastal areas, the simulations generally underestimate daily maximum temperatures. This underestimation is likely contributing to the southern cold bias of monthly mean temperatures. Similarly, the time-mean warm biases over the northern latitudes (Figure 9) are partly due to overestimation of extreme hot temperatures. As an added value of high resolution, ne30x8-t shows the smallest underestimation in the south in all seasons. For ne30-n, ne30x4-t, and ne30x8-t, the respective seasonal biases are as follows: DJF: 3.64, 3.51, and 2.97°C; MAM: 2.83, 2.49, and 2.43°C; JJA: 3.05, 2.92, and 2.87°C; and SON: 3.17, 3.07, and 3.08°C. Increasing resolution from 1° to 0.25° (from ne30-n to ne30x4-t) decreases biases with the greatest improvement occurring in MAM. Although warm biases over the central-eastern Europe increase with higher resolution, overall, ne30x8-t performs the best in terms of daily maximum temperature extremes with the smallest RMSE values except in fall (when it has a similar RMSE as in ne30x4-t). The largest improvement obtained by increasing resolution from 0.25° to 0.125° is seen in DJF.

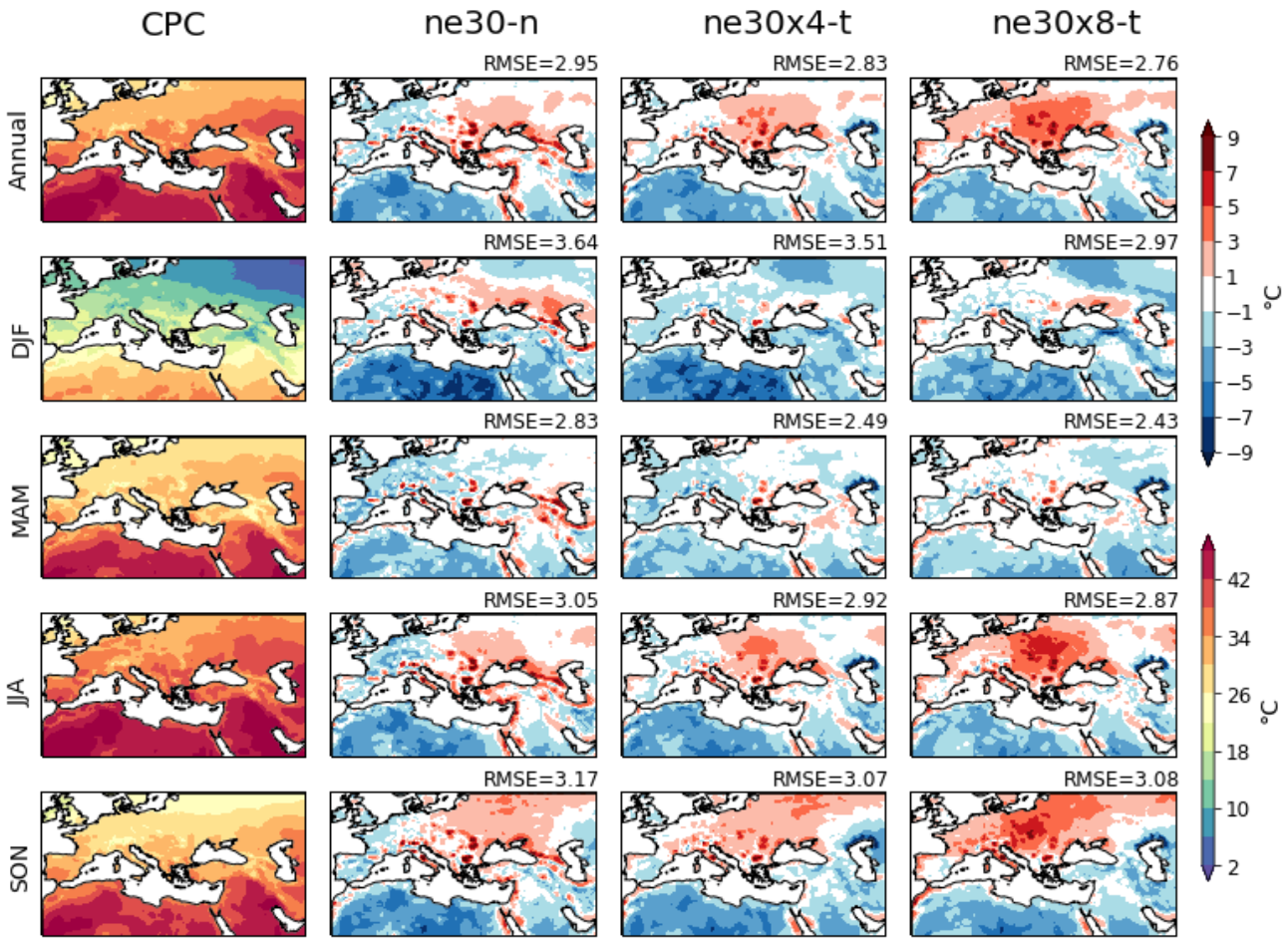

Figure 11. Distributions of the 99th percentile of daily Tmax from observations (CPC) (first column) and differences of simulations from observations. RMSEs are also given at the upper right of each panel. The observations and difference distributions use the lower and upper color bars, respectively.

3.3.2 Extreme Precipitation

Figure S9 depicts the observed (CPC) spatial distributions of the 99th percentile thresholds for daily precipitation over the study domain. The highest threshold values, well exceeding 80 mm/d, occur over high elevations (e.g., the Atlas Mountains, the European Alps, the Dinaric Alps, the Apennines, and the Zagros Mountains) as well as at the west coasts (e.g., the west coasts of Iberian Peninsula, Northern Africa, Croatia, and Anatolia) indicating the prominent influence of orography. There are apparently smaller precipitation rates (< 2 mm/d) over most of the southern regions (i.e., Northern Africa) consistent with this region's being located near the latitude belt of the descending branch of the Hadley cell.

In agreement with the previous studies which investigate extreme precipitation events in the Mediterranean region (e.g., Cavicchia et al., 2018; Dayan et al., 2015; Mastrantonas et al., 2020), western and eastern parts of the domain have different seasonalities, such that, the highest thresholds for the 99th percentile of daily precipitation are during fall and winter over the west

778 and east regions, respectively. As discussed in these studies, different physical mechanisms lead
779 to extreme precipitation events in different parts of the domain. The reader is referred to the
780 study by Dayan et al. (2015) for a review of large-scale circulation and regional to local
781 thermodynamic conditions leading to extreme precipitation events over the region. These
782 mechanisms include several atmospheric processes at different atmospheric scales, such as local
783 convection, upper synoptic-scale-level troughs, and mesoscale convective systems.

784 While temperature data are much more homogeneous in space and time, precipitation
785 data comprise strong spatiotemporal heterogeneity. Uncertainties related to evaluation data such
786 as the lack of enough stations over certain regions and observational undercatch caused by wind
787 effect particularly for solid precipitation (Rasmussen et al., 2012) further compromise the
788 inferences for model evaluations, even more so for the extreme precipitation. Hence, for a more
789 robust interpretation, the effects of increased resolution on the representation of extreme
790 precipitation are evaluated against two different datasets: CPC and E-OBS. Figure 12 and Figure
791 S10 show the observed spatial distributions of the 99th percentile thresholds of daily
792 precipitation and differences of the simulations from these observations over a region
793 encompassing western Europe and Northwestern Africa. This subregion is used here because it
794 includes high thresholds of extreme precipitation and has a complex topography. Furthermore, it
795 has a relatively high density of stations especially for E-OBS. Based on the RMSE values in
796 Figure 12, both VR simulations outperform the quasi-uniform 1° one in summer and fall and
797 0.125° resolution simulation (ne30x8-t) outperforms the 0.25° one in all seasons. Added value of
798 increasing resolution is apparent in the representation of summer extreme precipitation (RMSE
799 values are 6.09, 5.36, and 4.68 and 6.36, 5.63, and 5.02 mm/d for ne30-n, ne30x4-t, and ne30x8-
800 t, respectively). ne30x8-t has the smallest biases in summer among all model simulations. In
801 ne30x4-t and ne30x8-t, wet biases over high mountains including the Pyrennes and the European
802 Alps very likely exist due to systematic dry bias in the observations over high elevations which
803 significantly undermine an accurate assessment of improvements with high resolution by
804 artificially worsening the RMSE values (particularly in DJF). This is also supported by the lack
805 of such high wet biases for ne30-n highly possibly due to its smoother topography resolved
806 compared to VR configurations which decreases the duration snow cover persists. Even so, the
807 effect of increased resolution is clearly seen.

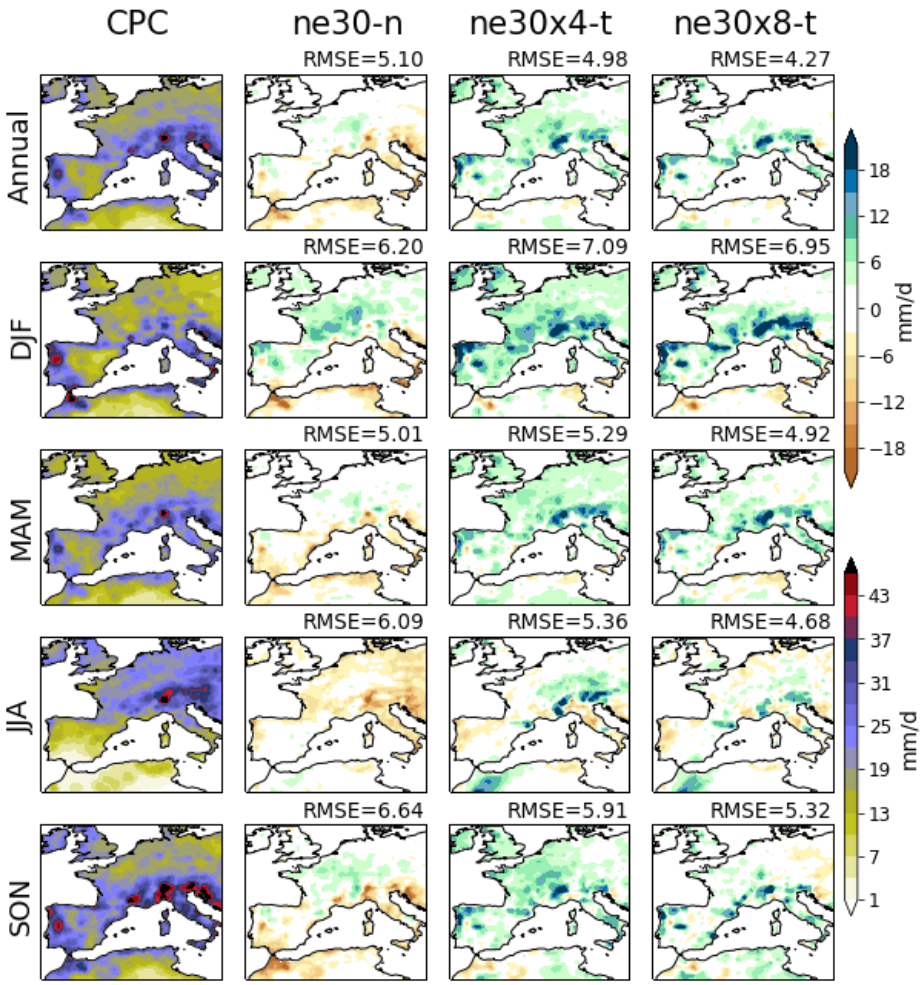

Figure 12. Distributions of the 99th percentile of daily precipitation from observations (CPC) (first column) and differences of simulations from observations (other columns) annually (first row) and seasonally (other rows). The observations and difference distributions use the lower and upper color bars, respectively.

Figure 13 displays the annual variability of extreme precipitation corresponding to the 99th percentile of daily precipitation, averaged over the subregions WEM, NEM, and EEM (see Figure 2). The grey and blue shadings correspond to the ensemble spread of ne30x4-t and ne30-n, respectively. The ensemble spread of ne30x4-t generally does not overlap with that of ne30-n (except in February for NEM and in January for EEM) which indicates that increasing resolution from 1° to 0.25° leads to a substantially different climate in terms of extreme precipitation. Single ne30x8-t simulation shows some values outside of the ensemble spread of ne30x4-t, indicating that much higher resolution is able to produce a relatively different climate in terms of extreme precipitation events. For a smaller percentile (i.e., 0.95), there is no such clear separation of 1° and 0.25° ensembles and no apparent departure of 0.125° simulation from the ensemble spread of 0.25° resolution (Figure S11). Therefore, these results suggest that increased resolution has greater implications for the very heavy precipitation events, i.e., at the 99th percentile as shown here.

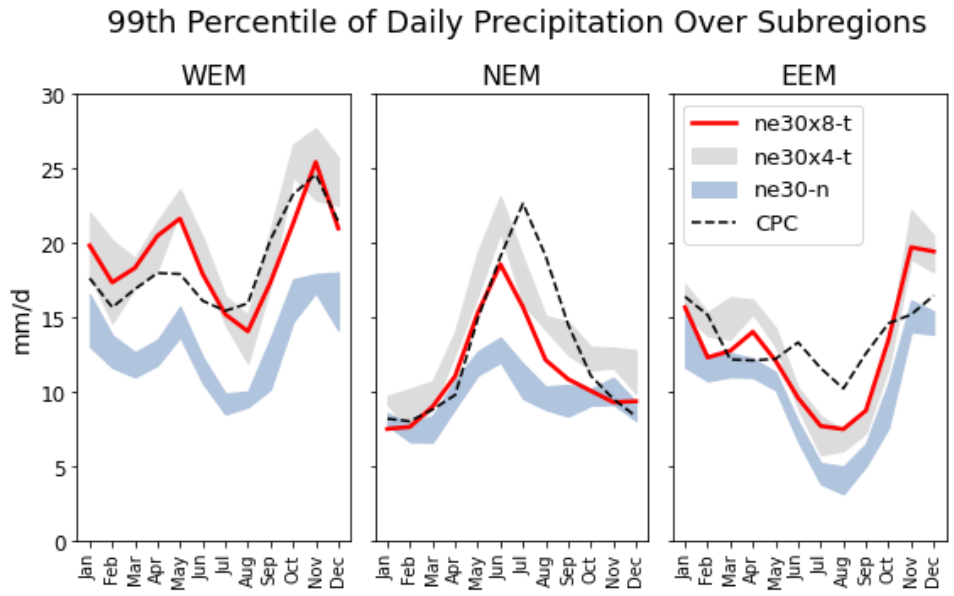

Figure 13 Annual cycles of the 99th percentile of daily precipitation over the subregions of WEM, NEM, and EEM. Grey and blue shadings correspond to the ensemble spread of ne30x4-t and ne30-n, respectively. The red line is for the single ne30x8-t simulation.

Over western Europe (WEM), simulated extreme precipitation has two maximums, one (the lower maximum) during May and the other during November-December. The shape of simulated seasonal cycles in this region are similar to that of observation, whereas the difference of precipitation amounts between two maximums are larger for observations. Over eastern Europe (NEM), a distinct seasonality is present with summer being the season with the highest extreme precipitation amounts suggesting the dominance of convective processes in producing extreme precipitation in this area. This conclusion is also consistent with the more apparent departure of ne30x8-t simulation from the ne30x4-t ensemble among all subregions very likely because of the distinctive skill of ne30x8-t in resolving small-scale processes such as convection. Here, the reduction in the activity of convective scheme with increased resolution should be recalled which most likely prevents to see the actual improvement obtained with high resolution. Over NEM, the shape of annual cycle is better reproduced by VR simulations than the control simulation with a maximum during summertime while the control simulation has a smaller maximum during November. Over this subregion, the observed maximum occurs slightly later, during July. Over EEM, all simulations reproduce a similar shaped seasonal cycle with maximums during April and November and a minimum during July-August. Observed minimum is also seen in August. However, the shapes of simulated seasonal cycles are different from the observed one.

3.4 Impacts of Tuning

Figure 14 shows the differences of the simulations from observations (CERES EBAF) for SWCF annually and seasonally. Pattern correlations are between 0.87-0.94. The biases of Top of Atmosphere (TOA) shortwave cloud forcings remarkably worsen in ne30x4-n compared to ne30-n with the following RMSE values (in W/m^2): Annual: 7.39 vs. 9.92, DJF: 5.29 vs. 6.26, MAM: 11.35 vs. 13.98, JJA: 10.86 vs. 12.45, and SON: 7.34 vs. 10.19, respectively. With increased resolution, most prominent changes in the biases are the decrease in the area of the regions where

SWCF is underestimated by the model (e.g., Northwestern Europe, Central and Eastern Anatolia, the Arabian Peninsula) and expansion in the area overestimated with higher amplitudes (e.g., North of the Mediterranean Sea, the Black Sea, and the Caspian Sea) due to too thin clouds. Increasing horizontal resolution and/or reducing the physics time-step tends to thin the clouds, leading to a positive TOA energy imbalance (Herrington et al. 2022; Wijngaard et al. 2023). Parameter tuning was used to thicken the clouds in our VR simulations.

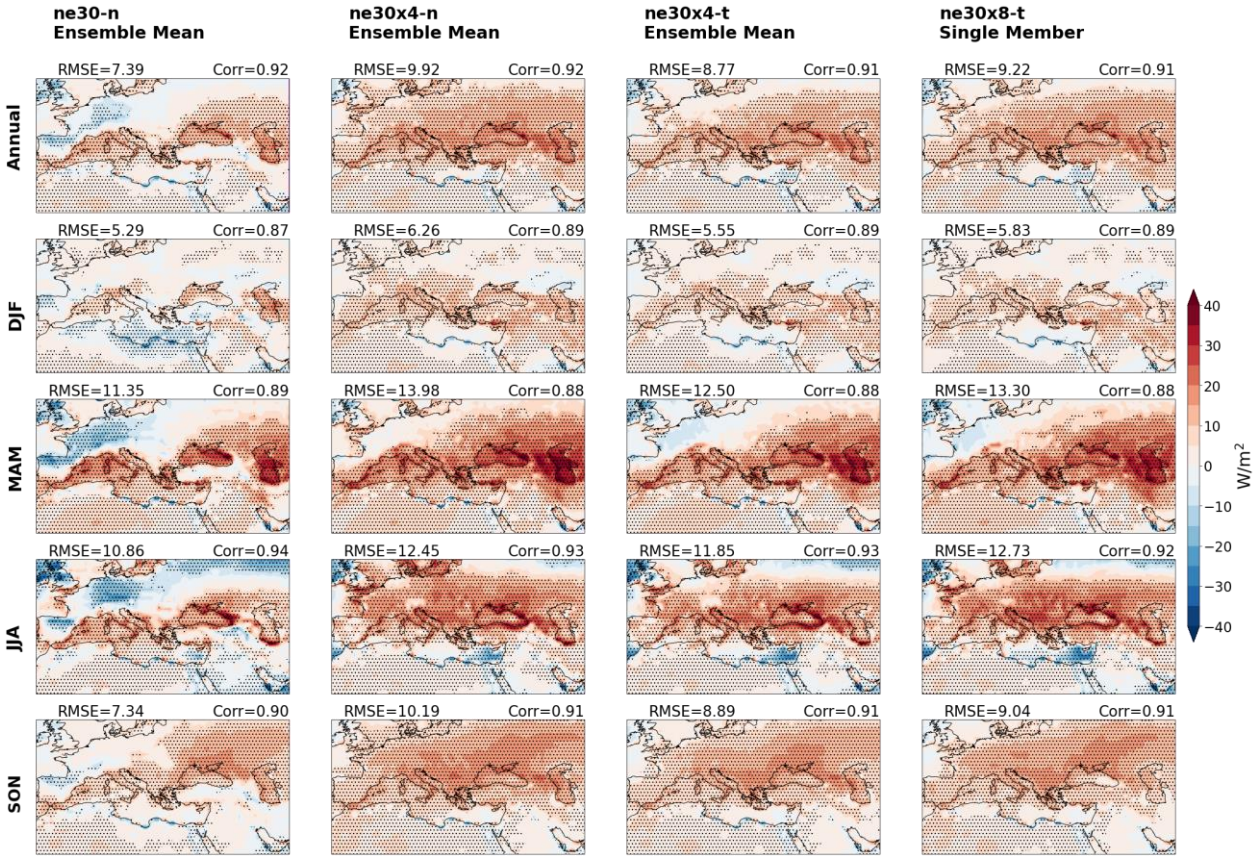

Figure 14. Annual (first row) and seasonal (other rows) differences of SWCF between simulations (ne30-n, ne30x4-n, ne30x4-t, and ne30x8-t in order) and observations. The observations are from CERES EBAF. RMSE and pattern correlations are given at the top of each panel. The dots indicate areas where the differences are statistically significant at the 95% level based on a two-sided Student's t-test.

Figure 15 shows the differences of the simulations from observations (CERES EBAF) for LWCF annually and seasonally. Pattern correlations are 0.71-0.93, slightly lower than that for SWCF. The biases of TOA longwave cloud forcings worsen in ne30x4-n compared to ne30-n with the following RMSE values (in W/m^2): Annual: 5.48 vs. 7.72, DJF: 6.83 vs. 8.32, MAM: 6.05 vs. 8.00, JJA: 6.07 vs. 7.63, and SON: 5.93 vs. 8.41, respectively. With increased resolution the area of the regions overestimated by the model (e.g., Central and Eastern Europe, Northeast of Anatolia, East of the Arabian Peninsula over the Persian Gulf) decreases and the areas underestimated (e.g., North of the Mediterranean Sea, the Black Sea, and the Caspian Sea in DJF, Northwest of Africa in SON) expands.

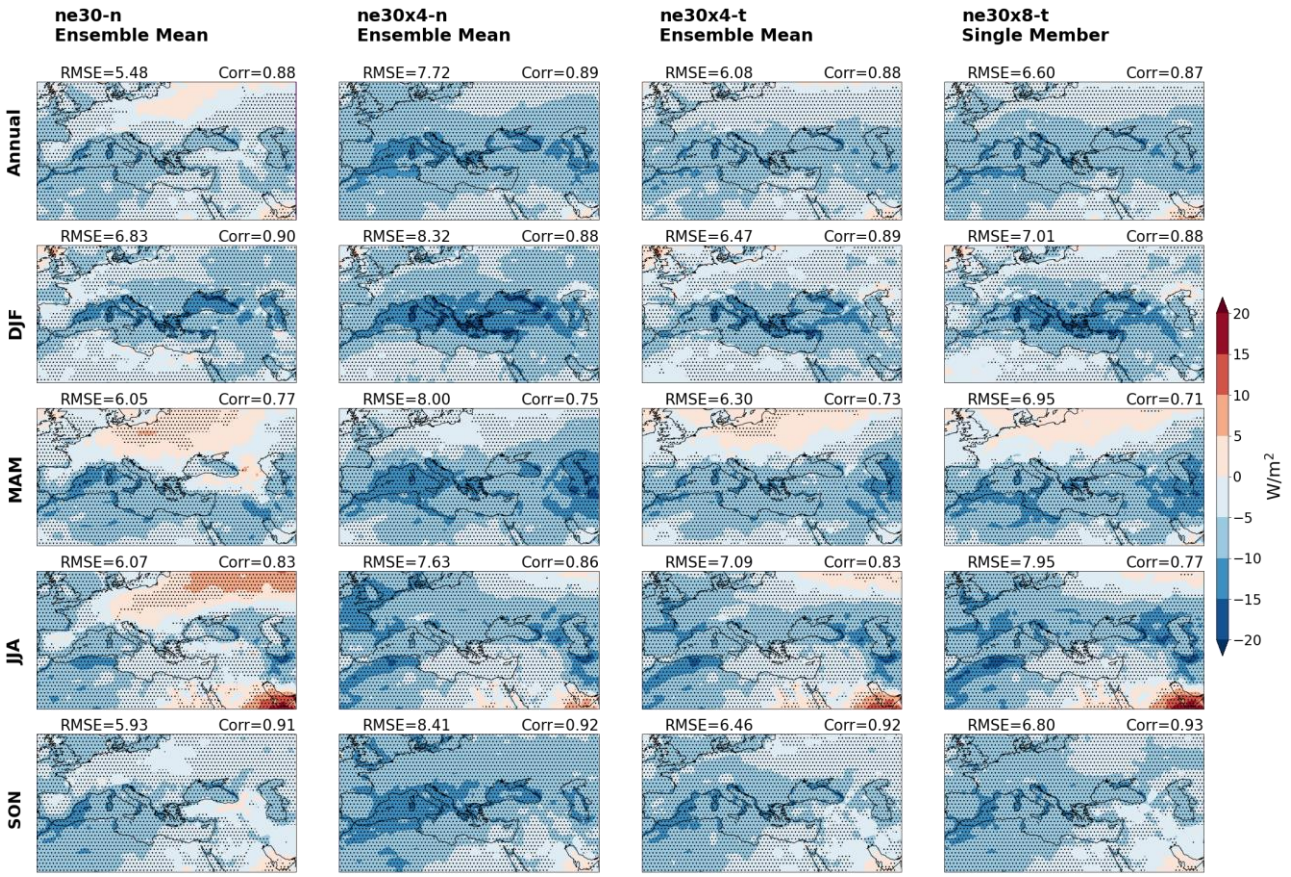

Figure 15. Same as Figure 14 but for LWCF.

With tuning, we target obtaining TOA longwave and shortwave radiation values which are in better agreement with observations (CERES EBAF dataset). We focus on the cloud forcing terms to investigate how tuning impacts the radiative effects of clouds. Although generally similar bias patterns remain, ne30x4-t simulations obtained by applying parameter tunings to ne30x4-n show improvements in the representation of SWCF and LWCF (check the columns 2 and 3 in Figures 14 and 15). With tuning, the signs and amplitudes of biases are restored to those in ne30-n to some degree. On the other hand, when resolution is increased once more from ne30x4-t to ne30x8-t, the RMSE values increase again although both simulations use identical tunings. This suggests that extra tunings are needed after increasing horizontal resolution further to recover this deterioration.

4 Conclusions

The primary objective of this study is to evaluate the performance of VR-CESM historical experiments in simulating the mean climatology and seasonal variability of surface temperature and precipitation over the Euro-Mediterranean region. The evaluation has been carried out by comparing variable resolution simulations with the quasi-uniform 1° control simulation and against observational and reanalysis datasets. This study also aims to explain the reasons for persistent biases in the simulations to guide better interpretation of results. The impacts of parameter tunings applied to the 0.25° VR simulation are also discussed with respect to changes in the longwave and shortwave cloud forcings.

Overall, VR simulations show more accurate representation of surface temperature and precipitation mainly due to better representations of topographical variance, including steep orographical gradients and land-sea contrasts, and of fine-scale processes such as orographic uplift and convection. The locations and expansions of upward and downward air motions are better simulated with high resolution, consistent with prior VR-CESM studies (Herrington et al., 2022; Morris et al., 2023). Therefore, added value of increased resolution is most evident at mountainous and coastal regions and for higher-moment climate statistics such as extreme events.

1° coarse resolution has large area-averaged surface temperature biases of approximately 2°C or more with the largest biases occurring in winter. There exist much higher warm biases over high mountains and coastal areas exceeding +6°C locally and in different seasons. With the resolution increased to 0.25°, biases significantly reduce particularly over areas with strong spatial gradients. These reductions clearly show the added-value of better topographic representation at higher resolutions. Simply increasing the resolution from 0.25° to 0.125° leads to further improvements, but not as much as seen upon increasing it from 1° to 0.25°, almost certainly because the topographical representations at 0.25°and 0.125° are quite similar whereas those of 1° are heavily smoothed. Still, 0.125° simulation shows the smallest temperature biases in all seasons in all the simulations.

Simulation of precipitation is more complicated than that of temperature because precipitation occurs as a result of many subgrid scale processes and accordingly its higher parameter dependency results in more uncertainty. On the other hand, increasing resolution from 1° to 0.25° improves the model performance. For precipitation, added value of increased resolution, again, is clearly seen in the areas with complex topography. Particularly, the reduction in precipitation biases on the windward/leeward sides of high mountains and on the coasts is a demonstration of higher skill of increased resolution in resolving adjacent topographical gradients and coastlines. Further increasing the resolution to 0.125° reduces the summertime biases whereas the biases in other seasons get slightly worse, mostly because of the lack of extra parameter tunings. Better summertime performance of 0.125° can be attributed to its ability to resolve more smaller scale processes related to convective activity.

Despite improvements, there are persistent temperature and precipitation biases across all simulations. We see a general warm (cold) bias over the northern (southern) areas of the region and a warm-dry bias over central and eastern Europe. These bias patterns are mainly related to land-atmosphere interactions. Another persistent bias is the overestimation of precipitation over northwest Europe especially in winter. High-resolution simulations show smaller winter wet biases than 1° control simulation in this region. This can be attributed to better representation of water vapor transport from the North Atlantic, as a demonstration of the ability of increased resolution in resolving dynamical processes driving precipitation, and also as a result of better topographical treatment which is more skillful in resolving orographic uplift on the windward side of the European Alps.

The added value of increased resolution is clearly evident in the representation of extreme maximum temperatures and precipitation. Generally, 0.25° resolution performs better than 1° and 0.125° resolution performs the best in terms of daily maximum temperature extremes. 0.25° resolution produces a different climate than 1° with respect to 99th percentile

941 precipitation and 0.125° has the smallest biases in summer among all the simulations, consistent
942 with the dominance of small scale processes in this season.

943 The results obtained by doubling the horizontal resolution from 0.25° to 0.125° should be
944 interpreted cautiously. First, this simulation consists of a single run and is not an ensemble as in
945 other simulations. So, the uncertainties caused by internal variability still exist without an
946 ensemble size large enough to produce a sufficient statistical sample. Internal variability
947 becomes increasingly important for processes occurring at smaller spatiotemporal scales
948 including the extreme events. Because, at small scales an additional spatial heterogeneity is
949 introduced leading to an additional internal variability which is partly averaged out at large
950 scales (Aalbers et al. 2018). Second, no specific tunings were applied over the 0.25° version
951 although timestep has been reduced. Therefore, the improvements seen are related to simply
952 increasing the horizontal resolution and further potential improvements are very likely offset by
953 lack of extra tunings. Third, 0.125° resolution has a topographical representation very similar to
954 that of 0.25°, therefore we should not expect additional improvements in the topography-induced
955 processes which can already be resolved by 0.25°. Even so, 0.125° simulation gives a clear
956 evidence of potential for further improvements in higher resolutions.

957 Shortwave and longwave cloud forcing biases that increase as a result of increasing
958 resolution from 1° to 0.25° are apparently corrected with tuning to some degree. However,
959 further increasing the resolution to 0.125° causes biases to get slightly worse again. Parameter
960 tunings do not result in a general improvement in the representation of surface temperature and
961 precipitation, as they target the cloud radiative forcing.

962 Significant difficulties arise in the interpretation of simulation results because of the
963 region's very complicated topography and climatologically different zones it encompasses.
964 Equally important is the fact that default model parameterizations are developed for use in coarse
965 resolution simulations, thus increasing resolution and accordingly decreasing the timestep lead to
966 some artificial biases including those caused by the reduction in the activity of the convective
967 scheme. Another source of artificial error, such as vastly overestimated precipitation over high
968 elevations with increased resolution, is due to deficiencies of the observational datasets. With the
969 caveat that the results must be interpreted cautiously, overall, variable resolution simulations
970 improve the representation of spatial distributions and seasonal evolution of T2m and
971 precipitation as well as the extreme precipitation and heat events over the Euro-Mediterranean
972 region. This makes VR-CESM a useful tool for evaluating the regional climate at high resolution
973 and for employing it for climate change studies for the region.

974

975

976

977

978

979

Acknowledgments

This study was supported by the 2247A National Outstanding Researchers Program of the Scientific and Technological Research Council of Türkiye (TUBITAK) under grant 120C137. The financial support from TUBITAK does not mean that the content of the publication reflects the approved scientific view of TUBITAK. Computer resources of the National Center for High Performance Computing of Türkiye (UHeM) (under grant number 1006542019) was used to simulate runs and analyze the data for this research. This material is also based upon work supported by the U.S. National Science Foundation (NSF) National Center for Atmospheric Research (NCAR), which is a major facility sponsored by the U.S. NSF under Cooperative Agreement 1852977. Some of the simulations were performed on the Cheyenne Supercomputer (doi:10.5065/D6RX99HX) at the NSF NCAR – Wyoming Supercomputing Center during Burcu Boza's visit to the NSF NCAR on the TUBITAK fellowship. The study was partly funded by the Scientific and Technological Research Council of Türkiye (TUBITAK) via an International Research Fellowship Programme for PhD Students (2214-A).

Open Research

The observation and reanalysis data sets used in this study are publicly available at their source repositories. The CPC Global Unified Gauge-Based Analysis of Daily Precipitation and CPC Global Unified Temperature data were provided by the NOAA PSL, Boulder, Colorado, USA, from their website at https://psl.noaa.gov. The CESM2.2 code is available at https://github.com/ESCOMP/CESM. Analyses are performed and figures are created by using Python (v3.8.13). The raw simulation data for the variables used to generate the figures are made available at Zenodo (DOIs: 10.5281/zenodo.10899785, 10.5281/zenodo.10916689, 10.5281/zenodo.10916873, 10.5281/zenodo.10928100, 10.5281/zenodo.10928245, 10.5281/zenodo.10928269, 10.5281/zenodo.10928342, 10.5281/zenodo.10929045, 10.5281/zenodo.10929342, 10.5281/zenodo.10929377, 10.5281/zenodo.10929387).

References

Aalbers, E., Lenderink, G., Meijgaard, E., & Hurk, B. (2018). Local-scale changes in mean and heavy precipitation in Western Europe, climate change or internal variability?. *Climate Dynamics*, 50. https://doi.org/10.1007/s00382-017-3901-9

Abiodun, B., Prusa, J., & Gutowski, W. (2008). Implementation of a non-hydrostatic, adaptive-grid dynamics core in CAM3. Part I: Comparison of dynamics cores in aqua-planet simulations. *Climate Dynamics*, 31, 795-810. https://doi.org/10.1007/s00382-008-0381-y

Bacmeister, J. T., Lauritzen, P. H., Dai, A., & Truesdale, J. E. (2012), Assessing possible dynamical effects of condensate in high resolution climate simulations, *Geophysical Research Letters.*, 39, *L04806*. https://doi.org/10.1029/2011GL050533

Batibeniz, F., Ashfaq, M., Onol, B., Turuncoglu, U., Mehmood, S., & Evans, K. (2020). Identification of major moisture sources across the Mediterranean Basin. *Climate Dynamics*, 54, 1-19. https://doi.org/10.1007/s00382-020-05224-3

Bergant, K., Belda, M., & Halenka, T. (2007). Systematic errors in the simulation of European climate (1961-2000) with RegCM3 driven by NCEP/NCAR reanalysis. *International Journal of Climatology*, 27, 455 - 472. https://doi.org/10.1002/joc.1413

Bogenschutz, P. A., Gettelman, A., Hannay, C., Larson, V. E., Neale, R. B., Craig, C., & Chen, C.-C. (2018). The path to CAM6: Coupled simulations with CAM5.4 and CAM5.5. *Geoscientific Model Development*, 11(1), 235–255. https://doi.org/10.5194/gmd-11-235-2018

Bozkurt, D., Ezber, Y., & Sen, O. (2019). Role of the East Asian trough on the eastern Mediterranean temperature variability in early spring and the extreme case of 2004 warm spell. *Climate Dynamics*. https://doi.org/10.1007/s00382-019-04847-5

Bozkurt, D., Turuncoglu, U., Sen, O., Onol, B., & Dalfes, N. (2012). Downscaled simulations of the ECHAM5, CCSM3 and HadCM3 global models for the eastern Mediterranean-Black Sea region: Evaluation of the reference period. *Climate Dynamics*, 39, 207-225. https://doi.org/10.1007/s00382-011-1187-x

Briegleb, B. P., & Light, B. (2007). A Delta-Eddington Mutiple Scattering Parameterization for Solar Radiation in the Sea Ice Component of the Community Climate System Model (No. NCAR/TN-472+STR). University Corporation for Atmospheric Research. https://doi.org/10.5065/D6B27S71

Cavicchia, L., Scoccimarro, E., Gualdi, S., Marson, P., Ahrens, B., Berthou, S., et al. (2018). Mediterranean extreme precipitation: a multi-model assessment. *Climate Dynamics*, 51, 901–913. https://doi.org/10.1007/s00382-016-3245-x

Chen, S.-C. (2002). Model mismatch between global and regional simulations. *Geophysical Research Letters*, 29(5). https://doi.org/10.1029/2001GL013570

Chen, M., Shi, W., Xie, P., Silva, V., Kousky, V., Higgins, W., & Janowiak, J. (2008). Assessing objective techniques for gauge-based analyses of global daily precipitation. Journal of Geophysical Research (Atmospheres), 113, 4110-. https://doi.org/10.1029/2007JD009132

Cornes, R. C., van der Schrier, G., van den Besselaar, E. J. M., & Jones, P. D. (2018). An ensemble version of the E-OBS temperature and precipitation data sets. *Journal of Geophysical Research: Atmospheres*, 123, 9391–9409. https://doi.org/10.1029/2017JD028200

Dafka, S., Xoplaki, E., Toreti, A., Zanis, P., Tyrlis, E., Zerefos, C., & Luterbacher, J. (2016). The Etesians: from observations to reanalysis. *Climate Dynamics*, 47. https://doi.org/10.1007/s00382-015-2920-7

Danabasoglu, G., Lamarque, J.-F., Bacmeister, J., Bailey, D. A., DuVivier, A. K., Edwards, J., et al. (2020). The Community Earth System Model Version 2 (CESM2). *Journal of Advances in Modeling Earth Systems*, 12, e2019MS001916. https://doi.org/10.1029/2019MS001916

1061 Danielson, J.J., & Gesch, D.B. (2011). Global multi-resolution terrain elevation data 2010 (GMTED2010): U.S.
1062 Geological Survey Open-File Report, 2011–1073, 26 p. https://doi.org/10.3133/ofr20111073

1063 Dayan, U., Nissen, K., & Ulbrich, U. (2015). Review Article: Atmospheric conditions inducing extreme
1064 precipitation over the eastern and western Mediterranean. *Natural Hazards and Earth System Sciences*, 15.
1065 https://doi.org/10.5194/nhess-15-2525-2015

1066 Dennis, J.M., Edwards, J., Evans, K.J., Guba, O., Lauritzen, P.H., Mirin, A.A., et al. (2012). CAM-SE: A scalable
1067 spectral element dynamical core for the Community Atmosphere Model. *The International Journal of High*
1068 *Performance Computing Applications*, 26, 74 - 89. https://doi.org/10.1177/1094342011428142

1069 Di Luca, A., Argüeso, D., Sherwood, S., & Evans, J. P. (2021). Evaluating precipitation errors using the
1070 environmentally conditioned intensity-frequency decomposition method. *Journal of Advances in Modeling Earth*
1071 *Systems*, 13, *e2020MS002447*. https://doi.org/10.1029/2020MS002447

1072 Fan, F., Bradley, R., & Rawlins, M. (2014). Climate change in the northeastern US: Regional climate model
1073 validation and climate change projections. *Climate Dynamics*, 43. https://doi.org/10.1007/s00382-014-2198-1

1074 Feser, F., Rockel, B., Storch, H., Winterfeldt, J., & Zahn, M. (2011). Regional Climate Models Add Value to Global
1075 Model Data: A Review and Selected Examples. *Bulletin of the American Meteorological Society*, 92(9*)*, 1181-1192.
1076 https://doi.org/10.1175/2011BAMS3061.1

1077 Fita, L., Romero, R., De Luque Söllheim, A., Emanuel, K., & Ramis, C. (2007). Analysis of the environments of
1078 seven Mediterranean tropical-like storms using an axisymmetric, nonhydrostatic, cloud resolving model. *Natural*
1079 *Hazards and Earth System Science*, 7. https://doi.org/10.5194/nhess-7-41-2007

1080 Flato, G., J. Marotzke, B. Abiodun, P. Braconnot, S.C. Chou, W. Collins, et al. (2013) Evaluation of Climate
1081 Models. In: Climate Change 2013: The Physical Science Basis. Contribution of Working Group I to the Fifth
1082 Assessment Report of the Intergovernmental Panel on Climate Change [Stocker, T.F., D. Qin, G.-K. Plattner, M.
1083 Tignor, S.K. Allen, J. Boschung, A. Nauels, Y. Xia, V. Bex and P.M. Midgley (eds.)]. Cambridge University Press,
1084 Cambridge, United Kingdom and New York, NY, USA.

1085 Fox-Rabinovitz, M., Côté, J., Dugas, B., Déqué, M., & McGregor, J. L. (2006) Variable resolution general
1086 circulation models: Stretched-grid model intercomparison project (SGMIP), *Journal of Geophysical Research*, 111,
1087 D16 104, https://doi.org/10.1029/2005JD006520

1088 Gettelman, A., Callaghan, P., Larson, V. E., Zarzycki, C. M., Bacmeister, J. T., Lauritzen, P. H., et al.
1089 (2018). Regional climate simulations with the Community Earth System Model. *Journal of Advances in Modeling*
1090 *Earth Systems*, 10, 1245–1265. https://doi.org/10.1002/2017MS001227

1091 Gettelman, A., Mills, M. J., Kinnison, D. E., Garcia, R. R., Smith, A. K., Marsh, D. R., et al. (2019). The whole
1092 atmosphere community climate model version 6 (WACCM6). *Journal of Geophysical Research:*
1093 *Atmospheres*, 124, 12380–12403. https://doi.org/10.1029/2019JD030943

1094 Gettelman, A., & Morrison, H.. (2015). Advanced Two-Moment Bulk Microphysics for Global Models. Part I: Off-
1095 Line Tests and Comparison with Other Schemes. *Journal of Climate*, 28, 1268-1287. https://doi.org/10.1175/JCLI-
1096 D-14-00102.1

1097 Giorgi F. (2006) Climate change hot-spots. *Geophysical Research Letters*, 33*:L08707*.
1098 https://doi.org/10.1029/2006GL025734

1099 Giorgi, F., Bi, X. & Pal, J.S. (2004). Mean, interannual variability and trends in a regional climate change
1100 experiment over Europe. I. Present-day climate (1961–1990). *Climate Dynamics*, 22, 733–756.
1101 https://doi.org/10.1007/s00382-004-0409-x

1102 Golaz, J.-C., Larson, V. E., & Cotton, W. R. (2002) A PDF-Based Model for Boundary Layer Clouds. Part I:
1103 Method and Model Description. *Journal of the Atmospheric Sciences*, vol. 59, no. 24, 3540–3551.
1104 https://doi.org/10.1175/1520-0469(2002)059<3540:APBMFB>2.0.CO;2

1105 Guba, O., Taylor, M., Ullrich, P., Overfelt, J., & Levy, M. (2014). The spectral element method (SEM) on variable-
1106 resolution grids: Evaluating grid sensitivity and resolution-aware numerical viscosity. *Geoscientific Model*
1107 *Development Discussions*, 7. https://doi.org/10.5194/gmdd-7-4081-2014

1108 Guo, Z., M. Wang, Y. Qian, V. E. Larson, S. Ghan, M. Ovchinnikov, et al. (2015). Parametric behaviors of CLUBB
1109 in simulations of low clouds in the Community Atmosphere Model (CAM), *Journal of Advances in Modeling Earth*
1110 *Systems*, 7, 1005–1025, https://doi.org/10.1002/2014MS000405

1111 Gutowski, W., Ullrich, P., Hall, A., Leung, L., O'Brien, T., Patricola, C., et al. (2020). The Ongoing Need for High-
1112 Resolution Regional Climate Models: Process Understanding and Stakeholder Information. *Bulletin of the American*
1113 *Meteorological Society* 101. https://doi.org/10.1175/BAMS-D-19-0113.1

1114 Harris, I., Jones, P.D., Osborn, T.J., & Lister, D.H. (2014). Updated high-resolution grids of monthly climatic
1115 observations – the CRU TS3.10 Dataset. *International Journal of Climatology*, 34, 623-
1116 642. https://doi.org/10.1002/joc.3711

1117 Harris, I., Osborn, T., Jones, P., & Lister, D. (2020). Version 4 of the CRU TS monthly high-resolution gridded
1118 multivariate climate dataset. *Scientific Data*, 7. https://doi.org/10.1038/s41597-020-0453-3

1119 Herrington, A. R., Lauritzen, P. H., Lofverstrom, M., Lipscomb, W. H., Gettelman, A., & Taylor, M. A. (2022).
1120 Impact of grids and dynamical cores in CESM2.2 on the surface mass balance of the Greenland Ice Sheet. *Journal of*
1121 *Advances in Modeling Earth Systems*, 14, e2022MS003192. https://doi. org/10.1029/2022MS003192

1122 Herrington, A., Lauritzen, P., Reed, K., Goldhaber, S., & Eaton, B. (2019). Exploring a lower resolution physics
1123 grid in CAM-SE-CSLAM. *Journal of Advances in Modeling Earth Systems*, 11.
1124 https://doi.org/10.1029/2019MS001684

1125 Herrington, A. & Reed, K. (2017). An Explanation for the Sensitivity of the Mean State of the Community
1126 Atmosphere Model to Horizontal Resolution on Aquaplanets. *Journal of Climate*, 30. https://doi.org/10.1175/JCLI-
1127 D-16-0069.1

1128 Herrington, A. R., & Reed, K. A. (2020). On resolution sensitivity in the Community Atmosphere Model. *Quarterly*
1129 *Journal Of The Royal Meteorological Society*, 146, 3789-3807. https://doi.org/10.1002/qj.3873

1130 Hersbach, H., Bell, B., Berrisford, P., Hirahara, S., Horányi, A., Muñoz Sabater, J., et al. (2020). The ERA5 global
1131 reanalysis. *Quarterly Journal of the Royal Meteorological Society*. https://doi. org/10.1002/qj.3803

1132 Huang, X., Rhoades, A. M., Ullrich, P. A., & Zarzycki , C. M. (2016). An evaluation of the variable-resolution-
1133 CESM for modeling California's climate, *Journal of Advances in Modeling Earth Systems*, 8, 345–369, https://doi.
1134 org/10.1002/2015MS000559

1135 Hunke, E. C., Lipscomb, W. H., Turner, A. K., Jeffery, N., & Elliott, S. (2015). CICE: The Los Alamos Sea Ice
1136 Model Documentation and Software User's Manual Version 5.1. T-3 Fluid Dynamics Group, Los Alamos National
1137 Laboratory, Tech. Rep. LA-CC-06-012.

1138 Hurrell, J.W., Hack, J., Shea, D., Caron, J., & Rosinski, J. (2008). A New Sea Surface Temperature and Sea Ice
1139 Boundary Dataset for the Community Atmosphere Model. *Journal of Climate*, 21. https://doi.
1140 org/10.1175/2008JCLI2292.1

1141 Insua-Costa, D., Senande-Rivera, M., Llasat, M.D., & Miguez-Macho, G. (2022). A global perspective on western
1142 Mediterranean precipitation extremes. *npj Climate and Atmospheric Science*, 5, 1-7. https://doi.org/10.1038/s41612-
1143 022-00234-w

1144 Iturbide, M., Gutiérrez, J., Alves, L., Bedia, J., Cerezo-Mota, R., Cimadevilla, E., et al. (2020). An update of IPCC
1145 climate reference regions for subcontinental analysis of climate model data: definition and aggregated datasets.
1146 *Earth System Science Data*, 12, 2959-2970. https://doi. org/10.5194/essd-12-2959-2020

1147 Kato, S., Rose, F., Rutan, D., Thorsen, T., Loeb, N., Doelling, D., et al. (2018). Surface irradiances of edition 4.0
1148 Clouds and the Earth's Radiant Energy System (CERES) Energy Balanced and Filled (EBAF) data product. *Journal*
1149 *of Climate*, 31. https://doi. org/10.1175/JCLI-D-17-0523.1

1150 Kotlarski, S., Keuler, K., Christensen, O, Colette, A., Deque, M., Gobiet, A., et al. (2014). Regional climate
1151 modeling on European scales: A joint standard evaluation of the EURO-CORDEX RCM ensemble. *Geoscientific*
1152 *Model Development*, 7, 1297-1333. https://doi. org/10.5194/gmd-7-1297-2014

1153 Kottek, M., Grieser, J., Beck, C., Rudolf, B., & Rubel, F. (2006). World Map of the Köppen-Geiger climate
1154 classification updated. *Meteorologische. Zeitschrift*, 15:259-263. https://doi.org/10.1127/0941-2948/2006/0130

Larson, V. E. (2017). CLUBB-SILHS: A parameterization of subgrid variability in the atmosphere. arXiv:1711.03675v2 [physics.ao-ph]. https://doi.org/10.48550/arXiv.1711.03675

Lauritzen, P. H., Bacmeister, J. T., Callaghan, P. F., & Taylor, M. A. (2015). NCAR_Topo (v1.0): NCAR global model topography generation software for unstructured grids. *Geoscientific Model Development*, 8(12), 3975–3986. https://doi.org/10.5194/gmd-8-3975-2015

Lauritzen, P. H., Nair, R. D., Herrington, A. R., Callaghan, P., Goldhaber, S., Dennis, J. M., et al. (2018). NCAR release of CAM-SE in CESM2.0: A reformulation of the spectral element dynamical core in dry-mass vertical coordinates with comprehensive treatment of condensates and energy. *Journal of Advances in Modeling Earth Systems*, 10(7), 1537–1570. https://doi.org/10.1029/2017MS001257

Lawrence, D. M., Fisher, R. A., Koven, C. D., Oleson, K. W., Swenson, S. C., Bonan, G., et al. (2019). The Community Land Model version 5: Description of new features, benchmarking, and impact of forcing uncertainty. *Journal of Advances in Modeling Earth Systems*, 11, 4245–4287. https://doi.org/10.1029/2018MS001583

Lin, Y., Dong, W., Zhang, M., Xie, Y., Xue, W., Huang, J., & Luo, Y. (2017). Causes of model dry and warm bias over central U.S. and impact on climate projections. *Nature Communications*, 8. https://doi.org/10.1038/s41467-017-01040-2

Lionello, P., Malanotte-Rizzoli, P., & Boscolo, R.(Eds). (2006). *Mediterranean Climate Variability* (pp 179–226). Amsterdam, NETHERLANDS: Elsevier.

Loeb, N., Doelling, D., Wang, H., Su, W., Nguyen, C., Corbett, J., et al. (2017). Clouds and the Earth's Radiant Energy System (CERES) Energy Balanced and Filled (EBAF) top-of-atmosphere (TOA) edition-4.0 data product. *Journal of Climate*, 31. https://doi.org/10.1175/JCLI-D-17-0208.1

Mastrantonas, N., Herrera-Lormendez, P., Magnusson, L., Pappenberger, F. & Matschullat, J. (2020). Extreme precipitation events in the Mediterranean: Spatiotemporal characteristics and connection to large-scale atmospheric flow patterns. *International Journal of Climatology*, 41, 4, 2710–2728. https://doi.org/10.1002/joc.6985

Matte, D., Laprise, R., Thériault, J. M., & Lucas-Picher, P. (2017). Spatial spin-up of fine scales in a regional climate model simulation driven by low-resolution boundary conditions. *Climate Dynamics*, 49(1–2), 563–574. https://doi.org/10.1007/s00382-016-3358-2

Mauritsen, T., Stevens, B., Roeckner, E., Crueger, T., Esch, M.,Giorgetta, M., et al. (2012). Tuning the climate of a global model. *Journal of Advances in Modeling Earth Systems*, 4. https://doi.org/10.1029/2012MS000154

McGregor, J. L. and Dix, M. R.: An updated description of the Conformal-Cubic Atmospheric Model (2008), in: High Resolution Numerical Modelling of the Atmosphere and Ocean, edited by: Hamilton, K. and Ohfuchi, W., Springer, New York, USA, 51– 76. https://doi.org/10.1007/978-0-387-49791-4_4

Morris, M., Kushner , P. J., Moore , G. W. K., & Mercan , O. M. (2023) Atmospheric Circulation Patterns Associated with Extreme Wind Events in Canadian Cities. *Journal of Climate*, 36, 4443–4460. https://doi.org/10.1175/JCLI-D-22-0719.1

Mueller, B., & Seneviratne, S. (2014). Systematic land climate and evapotranspiration biases in CMIP5 simulations: CMIP5 BIASES. *Geophysical Research Letters*, 41. https://doi.org/10.1002/2013GL058055

Onol, B., & Semazzi, F. (2009). Regionalization of Climate Change Simulations over the Eastern Mediterranean. *Journal of Climate*, 22,1944-1961. https://doi.org/10.1175/2008JCLI1807.1

Räisänen, J., Hansson, U., Ullerstig, A., Döscher, R., Graham, L., Jones, C., et al. (2004). European climate in the late twenty-first century: Regional simulations with two driving global models and two forcing scenarios. *Climate Dynamics*, 22, 13-31. https://doi.org/10.1007/s00382-003-0365-x

Rahimi, S. R., Wu, C., Liu, X., & Brown, H. (2019). Exploring a variable-resolution approach for simulating regional climate over the Tibetan Plateau using VR-CESM. *Journal of Geophysical Research: Atmospheres*, 124, 4490–4513. https://doi.org/10.1029/2018JD028925

1201 Rasmussen, R., Baker, B., Kochendorfer, J., Meyers, T. Landolt, S., Fischer, A., et al. (2012). How well are we
1202 measuring snow: the NOAA/FAA/NCAR winter precipitation test bed. *Bulletin of the American Meteorological*
1203 *Society*, 93. https://doi.org/10.1175/BAMS-D-11-00052.1

1204 Reed, K., Jablonowski, C., & Taylor, M. (2012). Tropical cyclones in the spectral element configuration of the
1205 Community Atmosphere Model. *Atmospheric Science Letters*, 13, 303-310. https://doi.org/10.1002/asl.399

1206 Rhoades, A., Huang, X., Ullrich, P., & Zarzycki, C. (2015). Characterizing Sierra Nevada Snowpack Using
1207 Variable-Resolution CESM. *Journal of Applied Meteorology and Climatology*, 55, *151023111431006*.
1208 https://doi.org/10.1175/JAMC-D-15-0156.1

1209 Rhoades, A., Jones, A., Srivastava, A., Huang, H., O'Brien, T., Patricola, C., et al. (2020). The Shifting Scales of
1210 Western US Landfalling Atmospheric Rivers Under Climate Change. *Geophysical Research Letters*, 47.
1211 https://doi.org/10.1029/2020GL089096

1212 Rhoades, A., Ullrich, P., Zarzycki, C., Johansen, H., Margulis, S., Morrison, et al. (2018). Sensitivity of Mountain
1213 Hydroclimate Simulations in Variable-Resolution CESM to Microphysics and Horizontal Resolution. *Journal of*
1214 *Advances in Modeling Earth Systems*. https://doi.org/10.1029/2018MS001326

1215 Ringler, T., Jacobsen, D., Gunzburger, M., Ju, L., Duda, M., & Skamarock, W. (2011). Exploring a Multiresolution
1216 Modeling Approach within the Shallow-Water Equations. *Monthly Weather Review*, 39, 3348-3368.
1217 https://doi.org/10.1175/MWR-D-10-05049.1

1218 Rodwell, M.J., & Hoskins, B.J. (1996). Monsoons and the dynamics of deserts. *Quarterly Journal of the Royal*
1219 *Meteorological Society*, 122, 1385-1404. https://doi.org/10.1002/qj.49712253408

1220 Rummukainen, M. (2015). Added value in regional climate modeling. *Wiley Interdisciplinary Reviews: Climate*
1221 *Change*, 7(1), 145–159. https://doi.org/10.1002/wcc.378

1222 Schmidt, G., Bader, D., Donner, L., Elsaesser, G., Golaz, J.-C., Hannay, C. et al.(2017). Practice and philosophy of
1223 climate model tuning across six US modeling centers. *Geoscientific Model Development*, 10, 3207-3223.
1224 https://doi.org/10.5194/gmd-10-3207-2017

1225 Sen, O., Ezber, Y., & Bozkurt, D. (2019). Euro-Mediterranean climate variability in boreal winter: a potential role of
1226 the East Asian trough. *Climate Dynamics*, 52. https://doi.org/10.1007/s00382-018-4573-9

1227 Simpson, I., Seager, R., Shaw, T., & Ting, M. (2015). Mediterranean Summer Climate and the Importance of
1228 Middle East Topography. *Journal of Climate*, 28, 1977-1996. https://doi.org/10.1175/JCLI-D-14-00298.1

1229 Small, R. J., Bacmeister, J., Bailey, D., Baker, A., Bishop, S., Bryan, F., et al. (2014). A new synoptic-scale
1230 resolving global climate simulation using the Community Earth System Model. *Journal of Advances in Modeling*
1231 *Earth Systems*, 6. https://doi.org/10.1002/2014MS000363

1232 Song, X., & Yu, L. (2017). Air-Sea heat flux climatologies in the Mediterranean Sea: Surface energy balance and its
1233 consistency with ocean heat storage. *Journal of Geophysical Research: Oceans*, 122.
1234 https://doi.org/10.1002/2016JC012254

1235 Taylor, M. A., & Fournier, A. (2010). A compatible and conservative spectral element method on unstructured
1236 grids. *Journal Of Computational Physics*, 229, 5879-5895. https://doi.org/10.1016/j.jcp.2010.04.008

1237 Tomita, H. (2008). A Stretched Icosahedral Grid by a New Grid Transformation. *Journal of the Meteorological*
1238 *Society of Japan*, 107-119. https://doi.org/10.2151/jmsj.86A.107

1239 Toreti, A., Xoplaki, E., Maraun, D., Kuglitsch, F. G., Wanner, H., & Luterbacher, J. (2010). Characterisation of
1240 extreme winter precipitation in Mediterranean coastal sites and associated anomalous atmospheric circulation
1241 patterns. *Natural Hazards and Earth System Sciences*. https://doi.org/10.5194/nhess-10-1037-2010

1242 Tuel, A., & Eltahir, E. A. B. (2021). Mechanisms of European Summer Drying under Climate Change. *Journal of*
1243 *Climate*, 34, 8913–8931. https://doi.org/10.1175/JCLI-D-20-0968.1

1244 Tyrlis, E., & Lelieveld, J. (2013). Climatology and Dynamics of the Summer Etesian Winds over the Eastern
1245 Mediterranean. *Journal of the Atmospheric Sciences*, 70, 3374–3396. https://doi.org/10.1175/JAS-D-13-035.1

Ullrich, P. (2014). Squadgen: Spherical quadrilateral grid generator. University of California, Davis, Climate and Global Change Group software.[Available online at http://climate.ucdavis.edu/squadgen.php.]

Van Kampenhout, L., Rhoades, A., Herrington, A., Zarzycki, C., Lenaerts, J., Sacks, W., & Van den Broeke, M. (2019). Regional grid refinement in an Earth system model: impacts on the simulated Greenland surface mass balance. *The Cryosphere*, 13, 1547-1564. https://doi.org/10.5194/tc-13-1547-2019

Vautard, R., Yiou, P., D'Andrea, F., de Noblet, N., Viovy, N., Cassou, C., et al. (2007). Summertime European heat and drought waves induced by wintertime Mediterranean rainfall deficit. *Geophysical Research Letters*, 34. https://doi.org/10.1029/2006gl028001

Wang, Y., Leung, L., McGregor, J., Lee, D.-K., Wang, W.-C., Ding, Y., & Kimura, F. (2004). Regional Climate Modeling: Progress, Challenges, and Prospects. *Journal of The Meteorological Society of Japan*, 8, 1599-1628. https://doi.org/10.2151/jmsj.82.1599

Wang, M., Ullrich, P., & Millstein, D. (2020). Future projections of wind patterns in California with the variable-resolution CESM: a clustering analysis approach. *Climate Dynamics*, 54, 2511–2531. https://doi.org/10.1007/s00382-020-05125-5

Wentz, F.J., Meissner, T., Gentemann, C. , Hilburn, K.A., & Scott, J. (2014) Remote Sensing Systems GCOM-W1 AMSR2 [Monthly] Environmental Suite on 0.25 deg grid, Version v08.2. Remote Sensing Systems, Santa Rosa, CA. Available online at www.remss.com/missions/amsr. [Accessed 20 July 2023].

Wijngaard, R., Herrington, A., Lipscomb, W., Leguy, G., & An, S.-I. (2023). Exploring the ability of the variable-resolution CESM to simulate cryospheric-hydrological variables in High Mountain Asia. *The Cryosphere*. https://doi.org/10.5194/tc-2022-256

Williamson, D. L. (2013). The effect of time steps and time-scales on parametrization suites. *Quarterly Journal of the Royal Meteorological Society*, 139(671), 548–560. https://doi.org/10.1002/qj.1992

Wu, C., Liu, X., Lin, Z., Rhoades, A. M., Ullrich, P. A., Zarzycki, C. M., Lu, Z., & Rahimi-Esfarjani, S. R. (2017). Exploring a variable-resolution approach for simulating regional climate in the Rocky Mountain region using the VR-CESM. *Journal of Geophysical Research: Atmospheres*, 122, 10,939–10,965. https://doi.org/10.1002/2017JD027008

Xie, S., Lin, W., Rasch, P. J., Ma, P. L., Neale, R., Larson, et al. (2018). Understanding cloud and convective characteristics in version 1 of the E3SM atmosphere model. *Journal of Advances in Modeling Earth Systems*, 10, 2618–2644. https://doi.org/10.1029/2018MS001350

Xie, P., Yatagai, A., Chen, M., Hayasaka, T., Fukushima, Y., Liu, C., & Yang, S. (2007) A gauge-based analysis of daily precipitation over East Asia. *Journal of Hydrometeorology*, 8, 607–626. https://doi.org/10.1175/JHM583.1

Xoplaki, E. (2002) *Climate variability over the Mediterranean* (PhD thesis). University of Bern, Switzerland.

Zarzycki, C., Jablonowski C., & Taylor, M. A. (2014). Using variable-resolution meshes to model tropical cyclones in the Community Atmosphere Model. *Monthly Weather Review*, 142, 1221–1239. https://doi.org/10.1175/MWR-D-13-00179.1

Zarzycki, C., Jablonowski, C., Thatcher, D., & Taylor, M. (2015). Effects of Localized Grid Refinement on the General Circulation and Climatology in the Community Atmosphere Model. *Journal of Climate*, 28, *150119122716002*. https://doi.org/10.1175/JCLI-D-14-00599.1

Zarzycki, C., Levy, M. N., Jablonowski, C., Overfelt, J. R., Taylor, M. A., & Ullrich, P. A. (2014). Aquaplanet experiments using CAM's variable-resolution dynamical core. *Journal of Climate*, 27(14), 5481–5503. https://doi.org/10.1175/JCLI-D-14-00004.1